Monthly Notices
of the
ROYAL ASTRONOMICAL SOCIETY

MNRAS **433,** 2706–2726 (2013) doi:10.1093/mnras/stt835
Advance Access publication 2013 June 27

Lyman break and ultraviolet-selected galaxies at $z \sim 1$ – I. Stellar populations from the ALHAMBRA survey

I. Oteo,[1,2]⋆ Á. Bongiovanni,[1,2] J. Cepa,[1,2] A. M. Pérez-García,[1,2,3] A. Ederoclite,[4] M. Sánchez-Portal,[3,5] I. Pintos-Castro,[1,2,15] R. Pérez-Martínez,[6] J. Polednikova,[1,2] J. A. L. Aguerri,[6] E. J. Alfaro,[7] T. Aparicio-Villegas,[7,16] N. Benítez,[7] T. Broadhurst,[8] J. Cabrera-Caño,[9] F. J. Castander,[10] M. Cerviño,[7] D. Cristobal-Hornillos,[7,4] A. Fernandez-Soto,[11,17] R. M. Gonzalez-Delgado,[7] C. Husillos,[7] L. Infante,[12] V. J. Martínez,[13,14] I. Márquez,[7] J. Masegosa,[7] I. Matute,[7] M. Moles,[7,4] A. Molino,[7] A. del Olmo,[7] J. Perea,[7] M. Pović,[7] F. Prada,[7] J. M. Quintana[7] and K. Viironen[4]

[1]*Instituto de Astrofísica de Canarias (IAC), E-38200 La Laguna, Tenerife, Spain*
[2]*Departamento de Astrofísica, Universidad de La Laguna (ULL), E-38205 La Laguna, Tenerife, Spain*
[3]*Asociación ASPID. Apartado de Correos 412, La Laguna, Tenerife, Spain*
[4]*Centro de Estudios de Física del Cosmos de Aragón, Plaza San Juan 1, Planta 2, E-44001 Teruel, Spain*
[5]*Herschel Science Centre (ESAC), Villafranca del Castillo, E-28692 Madrid, Spain*
[6]*XMM/Newton Science Operations Centre (ESAC), Villafranca del Castillo, Spain*
[7]*Instituto de Astrofísica de Andalucía (CSIC), Glorieta de la Astronomía s/n, E-18008 Granada, Spain*
[8]*School of Physics and Astronomy, Tel Aviv University, 69978 Tel Aviv, Israel*
[9]*Facultad de Física, Departamento de Física Atómica, Molecular y Nuclear, Universidad de Sevilla, Sevilla, Spain*
[10]*Institut de Ciencies de lEspai, IEEC-CSIC, Barcelona, Spain*
[11]*Instituto de Física de Cantabria (CSIC-UC), E39005, Santander, Spain*
[12]*Departamento de Astronomía, Ponticia Universidad Catolica, 7820436 Macul, Santiago, Chile*
[13]*Departament d' Astronomía i Astrofísica, Universitat de Valencia, Valencia, Spain*
[14]*Observatori Astronomic de la Universitat de Valencia, Valencia, Spain*
[15]*Centro de Astrobiología, INTA-CSIC, PO Box – Apdo. de correos 78, Villanueva de la Cañada, E-28691 Madrid, Spain*
[16]*Observatrio Nacional-MCT, Rua Jos Cristino, 77, CEP 20921-400, Rio de Janeiro-RJ, Brazil*
[17]*Unidad Asociada Observatorio Astronmico (Universitat de Valncia / IFCA-CSIC), Parc Cientfic UV, E-46980 Paterna, Spain*

Accepted 2013 May 9. Received 2013 May 9; in original form 2012 November 16

ABSTRACT

We take advantage of the exceptional photometric coverage provided by the combination of *GALEX* data in the ultraviolet (UV) and the ALHAMBRA survey in the optical and near-infrared to analyse the physical properties of a sample of 1225 *GALEX*-selected Lyman break galaxies (LBGs) at $0.8 \lesssim z \lesssim 1.2$ that are located in the COSMOS field. This is the largest sample of LBGs studied in this redshift range to date. According to a spectral energy distribution (SED) fitting with synthetic stellar population templates, we find that LBGs at $z \sim 1$ are mostly young galaxies with a median age of 341 Myr and have intermediate dust attenuation, $\langle E_s(B-V)\rangle \sim 0.20$. Owing to the selection criterion, LBGs at $z \sim 1$ are UV-bright galaxies and have a high dust-corrected total star formation rate (SFR), with a median value of $16.9\,\mathrm{M}_\odot\,\mathrm{yr}^{-1}$. Their median stellar mass is $\log(M_*/\mathrm{M}_\odot) = 9.74$. We find that the dust-corrected total SFR of LBGs increases with stellar mass and that the specific SFR is lower for more massive galaxies (downsizing scenario). Only 2 per cent of the galaxies selected through the Lyman break criterion have an active galactic nucleus nature. LBGs at $z \sim 1$ are located mostly over the blue cloud of the colour–magnitude diagram of galaxies at their redshift, with only the oldest and/or the dustiest deviating towards the green valley and red

⋆E-mail: ioteo@iac.es

sequence. Morphologically, 69 per cent of LBGs are disc-like galaxies, with the fractions of interacting, compact, or irregular systems being much lower, below 12 per cent. LBGs have a median effective radius of 2.5 kpc, and larger galaxies have a higher total SFR and stellar mass. Compared with their high-redshift analogues, we find evidence that LBGs at lower redshifts are larger, redder in the UV continuum, and have a major presence of older stellar populations in their SEDs. However, we do not find significant differences in the distributions of stellar mass or dust attenuation.

Key words: galaxies: evolution – galaxies: photometry – galaxies: high-redshift – galaxies: star formation – cosmology: observations – ultraviolet: galaxies.

1 INTRODUCTION

Much effort has been devoted over the last decades to searching for high-redshift star-forming (SF) galaxies. Different selection criteria select distinct kinds of galaxies. Among these criteria, the most successful and most commonly used are the Lyman-alpha and the Lyman break techniques, which pick up the so-called Lyman-alpha emitters (LAEs) and Lyman break galaxies (LBGs), respectively. The Lyman-alpha technique is based on looking for a Lyman-alpha emission in the redshifted optical spectrum of galaxies by employing a combination of narrow- and broad-band filters. Specifically, the narrow-band filter is used to isolate the Lyα line, and the broad-band one(s) to constrain its nearby continuum (Cowie & Hu 1998; Gronwall et al. 2007; Gawiser et al. 2006; Ouchi et al. 2008, 2010; Bongiovanni et al. 2010; Shioya et al. 2009). The choice of the central wavelength of the narrow-band filter determines the redshift of the selected LAEs, which have been searched for, found, and analysed from $z \sim 2.0$ up to $z \sim 7$ and beyond (Gawiser et al. 2006; Murayama et al. 2007; Nilsson et al. 2007, 2009; Pirzkal et al. 2007; Ouchi et al. 2008; Finkelstein et al. 2009b; Guaita et al. 2011; Hibon et al. 2011, 2012; Oteo et al. 2011, 2012a,b). LBGs are found by employing a combination of broad-band filters that sample the red-ward and blue-ward zones of the redshifted Lyman break of galaxies, located at 912 Å in the rest-frame (Madau et al. 1996; Steidel et al. 1996, 2003). The choice of the red-ward and blue-ward filters determines the location in wavelength of the Lyman break and, consequently, the redshift of the selected galaxies. Many samples of LBGs have been found and examined at different redshifts, mostly at $z \gtrsim 3$ (Madau et al. 1996; Steidel et al. 1996, 1999, 2003; Stanway, Bunker & McMahon 2003; Bunker et al. 2004; Giavalisco et al. 2004; Iwata et al. 2007; Verma et al. 2007). At $z \lesssim 3$ the number of LBGs reported and studied is much lower than that at higher redshifts (Burgarella et al. 2006, 2007; Ly et al. 2009, 2011; Basu-Zych et al. 2011; Hathi et al. 2010, 2013; Nilsson et al. 2011; Haberzettl et al. 2012; Chen et al. 2013), despite the fact that this redshift range is quite important as it is thought that the peak of the cosmic star formation of the Universe took place in that epoch.

Apart from the Lyα and Lyman break techniques, various other methods have been used for selecting high-redshift galaxies in the literature. Adelberger et al. (2004) defined various colour selection criteria that employ several combinations of optical colours to select galaxies at different redshifts: *GRi* for sources within $0.85 \lesssim z \lesssim 1.15$, *GRz* for $1.0 \lesssim z \lesssim 1.5$, and U_n*GR* for $1.4 \lesssim z \lesssim 2.1$ and $1.9 \lesssim z \lesssim 2.7$. The galaxies selected in this way have been traditionally called BM/BX galaxies. Another ground-based optical colour selection criterion is the *BzK* method, which aims to find galaxies in the redshift range $1.4 \lesssim z \lesssim 2.5$ and to classify them as SF or passively evolving systems (Daddi et al. 2004). Both kinds of galaxies are often associated with LBGs. Haberzettl et al. (2012) found that near-ultraviolet (NUV) data provide a greater efficiency for selecting SF galaxies. Furthermore, they reported that, although the BM/MX and *BzK* techniques are very efficient for detecting sources within $1.0 \lesssim z \lesssim 3.0$, they are biased against those SF galaxies that are more massive and contain a noticeable amount of red stellar populations. Haberzettl et al. (2012) argue that, therefore, a NUV-based LBG selection criterion is more appropriate for comparisons with the populations found at $z \gtrsim 3.0$.

The physical properties of high-redshift SF galaxies have been traditionally analysed by fitting their observed spectral energy distributions (SEDs) built from their photometric data[1] to SED templates obtained from stellar population models (such as Bruzual & Charlot 2003, hereafter BC03; Lai et al. 2008; Gawiser et al. 2007; Nilsson et al. 2007, 2009; Yabe et al. 2009; Finkelstein et al. 2008, 2009a,c, 2010a; Magdis et al. 2010). This procedure, in principle, enables the determination of age, dust attenuation, star formation rate (and history), metallicity and stellar mass. This is because the SED obtained in stellar population models depends on (among others) all these parameters. In practice, however, this procedure has several limitations. For example, metallicity does not have a strong influence on the shape of the rest-frame optical SEDs and, therefore, its determination from SED-fitting suffers from large uncertainties. On the other hand, the degeneracy between dust attenuation and age and that between star-formation history (SFH) and age mean that the three parameters are difficult to constrain accurately at the same time. With a good wavelength coverage of the UV continuum and the 4000-Å Balmer break it is feasible to improve the determination of the SED-derived dust attenuation and stellar age. However, dust attenuation would still suffer from uncertainties, and the only way to obtain accurate values is by employing direct far-infrared (FIR) detections around the dust emission peak (Burgarella et al. 2011; Oteo et al. 2013a). Despite these caveats, many previous works have analysed the physical properties of LBGs at different redshifts by employing an SED-fitting method, as it is the only way to analyse their properties with large samples of galaxies. At $z \sim 5$, LBGs have been reported to be much younger (<100 Myr) and to have lower stellar masses (10^9 $M_\odot$) than their analogues at $z \sim 2.0$–3.0 in a similar rest-frame UV luminosity range (Verma et al. 2007; Yabe et al. 2009; Haberzettl et al. 2012).

Most previous works have focused on LBGs that are located at $z \gtrsim 3$, where the Lyman break is shifted to the optical and can be sampled with filters in ground-based telescopes. At $z \lesssim 2$, the Lyman break is located in the UV, and LBGs can be found only through observations from space, for example with *GALEX*

[1] In this work we use the term SED to refer to a set of photometric points. However, it should be noted that SED is also applied to spectroscopic data in many works. Some of the limitations quoted here for the SED-fitting technique apply only to photometric SEDs, and not to spectroscopic ones.

(Burgarella et al. 2006, 2007; Haberzettl et al. 2012), *HST* and UVIS filters (Hathi et al. 2013), or with the *Swift* satellite (Basu-Zych et al. 2011). In this work, we aim to analyse the physical properties of a sample of 1225 *GALEX*-selected LBGs at $z \sim 1$ located in the COSMOS field by using data from the Advanced Large, Homogeneous Area Medium Band Redshift Astronomical (ALHAMBRA) survey (Moles et al. 2008), which covers the optical range with 20 medium-band filters (width about 300 Å) and the NIR with the traditional *JHKs* broad-band filters. The combination of the ALHAMBRA survey with observations in other wavelengths (*GALEX* and IRAC) allows an unprecedented coverage of the UV continuum and optical Balmer break. This can disrupt some of the degeneracies outlined above and provide more accurate results for the SED-derived physical properties. Because we study LBGs at $z \sim 1$, their observed fluxes are high enough that the photometry has a good signal-to-noise ratio. These two facts (exceptional coverage of the SED and the high signal-to-noise ratio) are not usually achieved at higher redshifts. This emphasizes the importance of studying intermediate-redshift LBGs.

The paper is organized as follows. In Section 2 we present the data sets employed both in the UV with *GALEX* and in the optical-to-NIR with the ALHAMBRA survey. In Section 3 we combine these two data sets to build a general sample of UV-selected galaxies at $0 \lesssim z \lesssim 2$. In Section 3 we also explain how we carry out the SED fits using BC03 templates for these UV-selected sources with the aim of obtaining their photometric redshift, rest-frame UV luminosity, and other physical properties such as dust attenuation, age and stellar mass. In Section 4 we define the selection criterion adopted in this work to look for LBGs at $z \sim 1$. The SED-derived physical properties of the selected LBGs are discussed in Section 5. The morphology and physical sizes of the LBGs studied are analysed in Section 6, and in Section 7 we show their location in the colour–magnitude diagram (CMD). In Section 8 we compare the properties of our *GALEX*-selected LBGs with those reported in previous works for LBGs at higher redshifts. Finally, we summarize the main conclusions of the work in Section 9.

Throughout this paper we assume a flat universe with $(\Omega_{\rm m}, \Omega_{\Lambda}, h_0) = (0.3, 0.7, 0.7)$, and all magnitudes are listed in the AB system (Oke & Gunn 1983).

2 DATA SETS

On the UV side we use data coming from observations of the COSMOS field with the *GALEX* satellite (Martin et al. 2005) in both the NUV and far-ultraviolet (FUV) bands as part of the Deep Imaging Survey (PI: D. Schiminovich). *GALEX* catalogues were created by using the EM-algorithm (Guillaume et al. 2006), aimed at resolving blended objects in the far- and the near-UV using the information (position and shape) available from existing, well-resolved catalogues on the visible range. In the concrete case of the COSMOS field, the prior optical photometric information corresponds to a *u**-band mosaic (and its SExtractor-derived catalogue) based on CFHT-*u** observations. With a list of optical prior positions, the algorithm measures their UV fluxes on the *GALEX* images by adjusting a *GALEX* point spread function model. The algorithm was run on the four NUV and the four FUV *GALEX* images covering the COSMOS field obtained as a product of the *GALEX* pipeline processing, version 1.61.

On the optical and NIR side we use the ALHAMBRA survey (Moles et al. 2005, 2008), which employs a set of 20 equal-width (∼300-Å) medium-band filters covering the optical range from 3500 to 9700 Å plus the traditional *JHKs* broad-band NIR filters to observe a region of 4 square degrees distributed into eight distinct fields. Among them, we focus our work on the COSMOS field owing to the wealth of photometric and spectroscopic data in the UV, optical, NIR and other wavelengths. The observations were carried out with the 3.5-m telescope of the Calar Alto Observatory using the wide-field camera LAICA in the optical and the OMEGA-2000 camera in the NIR. The optical filter system adopted in ALHAMBRA was set with the aim of optimizing the output of the survey in terms of the $z_{\rm phot}$ accuracy (Benítez et al. 2009). The simulations performed in Benítez et al. (2009) relating the image depth, $z_{\rm phot}$ accuracy, and number of filters indicate that the filter system of ALHAMBRA enables a $z_{\rm phot}$ precision, for normal SF galaxies, that is three times better than that for traditional 4–5 broad-band filter sets. In addition, the complementary usage of NIR data improves the determination of photometric redshifts. In this work we have used the catalogues coming from the Internal Data Release 3. The data reduction and the construction of the catalogues were carried out by the ALHAMBRA team. Because the ALHAMBRA survey performs observations in 23 filters, it is necessary to work with care when defining the detection of objects. With the aim of not biasing the detection to any particular kind of object as a consequence of the selection in a single band, a special technique was employed. It is based on creating a deep detection image built as the sum of the individual frames with the highest efficiencies. This includes the filters centred between 457 and 829 nm. The photometry of the sources was obtained by running SExtractor in its dual mode. The deep image is used for source detection, and the photometry is then extracted in each individual frame. As a result, the average depth (for 3σ detections) is 24.5 and 22 mag in the optical and NIR, respectively. In this work we employ the SExtractor-derived AUTO_MAG as the best approximation to the total magnitude for all calculations. The characterization in the optical range of the ALHAMBRA photometric system can be found in Aparicio Villegas et al. (2010), and the NIR number counts of one of the fields are presented in Cristóbal-Hornillos et al. (2009). Further details on the quality of the data, the reduction process, the depth, etc. will be published in Husillos et al. (in preparation). We note that the characterization of ALHAMBRA filters (complete wavelength coverage with almost no overlapping filters) provides an SED that can be considered as a low-resolution optical spectrum of the observed sources. It should be noted that the Lyman break selection that will be employed in this work is based purely on UV *GALEX* data, whereas the ALHAMBRA survey is used in the analysis of their SED-derived physical properties.

3 *GALEX* AND ALHAMBRA DATA: UV-SELECTED GALAXIES AND SED FITTING

The LBGs that will be studied in this work are taken from a multiwavelength catalogue of UV-selected SF galaxies that we build by combining the *GALEX* observations with the data coming from the ALHAMBRA survey: we look for *GALEX* detections around 2 arcsec of the optical position of the sources in the ALHAMBRA survey and retain only those galaxies that have, at least, a detection in the NUV band. This produces a sample of 39 734 UV-selected sources for which we have photometric information from the UV to the NIR.

With the aim of obtaining the photometric redshifts and the physical properties of those UV-selected sources we fit their observed fluxes to BC03 templates with the Zurich Extragalactic Bayesian Redshift Analyzer (ZEBRA, Feldmann et al. 2006) code, which, in its maximum-likelihood mode, employs a χ^2 minimization algorithm

over the templates to find the one that best fits the observed SED of each input object. We build a set of BC03 templates associated with various physical properties of galaxies by using the software GALAXEV. In this process we adopt a Salpeter (1955) initial mass function (IMF) distributing stars from 0.1 to 100 $M_\odot$ and select a fixed value for the metallicity of $Z = 0.2\,Z_\odot$. We consider values of age from 1 Myr to 7 Gyr, in steps of 10 Myr from 1 Myr to 1 Gyr and in steps of 100 Myr from 1 Gyr to 7 Gyr. Dust attenuation is included in the templates via the Calzetti et al. (2000) law and parametrized through the colour excess in the stellar continuum, $E_s(B-V)$. We select values for $E_s(B-V)$ ranging from 0 to 0.7 in steps of 0.05. We include intergalactic medium (IGM) absorption, adopting the Madau (1995) prescription. Regarding the SFR, we adopt time-constant models. In this case, different values of the SFR do not change the shape of the templates, and the SFR can be obtained using the Kennicutt (1998) calibration:

$$\mathrm{SFR_{UV,uncorrected}}[M_\odot \mathrm{yr}^{-1}] = 1.4 \times 10^{-28} L_{1500}, \quad (1)$$

where L_{1500} is the rest-frame UV luminosity at 1500 Å. The L_{1500} is obtained for each galaxy by convolving its best-fitting template with a top-hat filter (300 Å width) centred in the 1500 Å rest-frame. It should be noted that, throughout this work, we distinguish between L_{UV} defined in a νL_ν way (units of erg s^{-1}) and L_{1500} considered in L_ν units (erg s^{-1} Hz^{-1}). The SFR derived from equation (1) is uncorrected for the attenuation that dust produces in the SEDs of galaxies. In order to obtain an estimation of the dust-corrected total SFR we have to introduce into equation (1) the dust-corrected L_{1500}. It is obtained from L_{1500} by multiplying it by the dust correction factor $10^{0.4A_{1500}}$, where A_{1500} is the dust attenuation at 1500 Å. The values of A_{1500} are obtained from the SED-derived $E_s(B-V)$ assuming the Calzetti et al. (2000) law. Once both the age and dust-corrected total SFR are known for each source, and according to the assumed time-independent SFH, the stellar mass can be obtained from the product of the two quantities.

In this work we also analyse the UV continuum slope, β, of our UV-selected galaxies (see for example Calzetti, Kinney & Storchi-Bergmann 1994). This parameter is important in the study of how galaxies form/grow, as it is related to age, metallicity, stellar IMF, and, most importantly, dust attenuation. Furthermore, UV colours seem to be related to the UV luminosities of SF galaxies (Bouwens et al. 2009, 2010a, 2011) and are easier to measure than optical rest-frame colours in high-redshift galaxies, for which IRAC detections would be mandatory. The combination of the *GALEX* photometry and the bluest optical bands of the ALHAMBRA survey provides a good sampling of the UV continuum at $z \sim 1$, the redshift range in which our LBGs are located, as can be seen in the SED fits shown in Fig. 1. Different works employ different methods to obtain the UV continuum slope of galaxies in different redshift ranges, the most popular and traditionally used being that in which β is quantified by using two broad-band filters that sample two zones of the observed UV continuum (Meurer et al. 1997; Kong et al. 2004; Hathi, Malhotra & Rhoads 2008; Overzier et al. 2008; Bouwens et al. 2010b; Finkelstein et al. 2010b; Dunlop et al. 2012). In other works, β is obtained by using a power-law fit to the observed fluxes of the studied galaxies, using filters that sample the same zone of the SED at different redshifts (Bouwens et al. 2012). In our work, we obtain β for each galaxy by fitting the UV continuum of its best-fitting template with a power law in the form $f_\lambda \sim \lambda^\beta$ (Calzetti et al. 1994). In this process we employ the rest-frame wavelength range 1300 Å $\lesssim \lambda \lesssim$ 3000 Å. This range contains all the windows defined in Calzetti et al. (1994) in their definition of the UV continuum slope. This approach has the advantage of using all the available fluxes of each source, resulting in more robust signal-to-noise ratio determinations. The method employed here is similar to that used by Finkelstein et al. (2012) in their study of the redshift evolution of the UV continuum slope from $z \sim 8$ to $z \sim 4$. In that work, they present some illustrative examples showing the differences in the UV continuum slope when using the different techniques.

In an SED-fitting procedure, the reliability of the results, that is, the similarity between the observed SED and that represented by its best-fitting template, is related to the χ^2 value of the fits. Here we define the reduced χ^2, χ^2_r of each best-fitting template as the ratio between its χ^2 and the number of filters minus one employed in the fit, $\chi^2_\mathrm{r} = \chi^2/(N-1)$ (see for example de Barros, Schaerer & Stark 2012). From a visual inspection of the SED-fitting results, we consider that the BC03 templates truly represent the observed SED for each galaxy when $\chi^2_\mathrm{r} < 10$ (for some examples of χ^2 values and the quality of the fittings see Fig. 1). Imposing $\chi^2_\mathrm{r} < 10$ to the fittings of the whole sample of 39 754 UV-selected galaxies, we end up with a robust sample of 35 810 galaxies. From now on, only sources with $\chi^2_\mathrm{r} < 10$ are considered.

The χ^2_r values depend on the observed fluxes and also on their photometric uncertainties. In this way, if a galaxy has a photometry with high photometric errors, the χ^2_r might be low even when its best-fitting template does not represent its observed SED properly. Therefore, a low value of χ^2_r can be due either to a good SED fit or to a bad SED fit with a photometry with high uncertainties. Thus, we should check the typical photometric errors of the ALHAMBRA photometry of our sources to analyse whether the low values of χ^2_r are due to truly accurate fits or are the consequence of high photometric errors. As an example, we show in the left panel of Fig. 2 the photometric errors in the ALHAMBRA filter centred at 613 nm of our sample of UV-selected sources for $0 \leq z \leq 2$ as a function of their observed magnitude in the same band. As expected, the photometric errors increase with the observed magnitude. If we consider that a fit is reliable for galaxies with typical photometric errors below 0.4 mag, we can trust only those SED-fitting results for galaxies typically brighter than about 25 mag. In the right panel of Fig. 2 we represent the observed magnitudes of the *GALEX*-selected LBGs that will be studied in this work. It can be seen that most of them meet the previous criterion, and therefore we can consider that the low values of χ^2_r are statistically attributable to good SED fits rather than to high photometric errors.

It should be noted that in this work we employ BC03 templates associated with a time-independent SFR. Other kinds of SFHs can be used, such as those that are exponentially declining or composed of bursts of star formation. In the first case, the SFR is characterized by the decaying time-scale, τ_{SFR}, which would be another parameter to obtain in the SED fitting, increasing the degrees of freedom in the process. Distinguishing between different kinds of SFHs is very challenging, even with a good photometric coverage of the SED of galaxies. Therefore, the results reported in this work should be understood as those derived with that choice of the SFR, but different values of the SED-derived parameters might be obtained if other temporal variations of the SFH were assumed. The analysis of the differences in the SED-fitting results depending on the assumption of the SFH will be studied in Section 5.3.

3.1 Photometric redshifts and their accuracy

The good coverage of the observed UV-to-NIR SEDs of galaxies provided by the ALHAMBRA survey in combination with

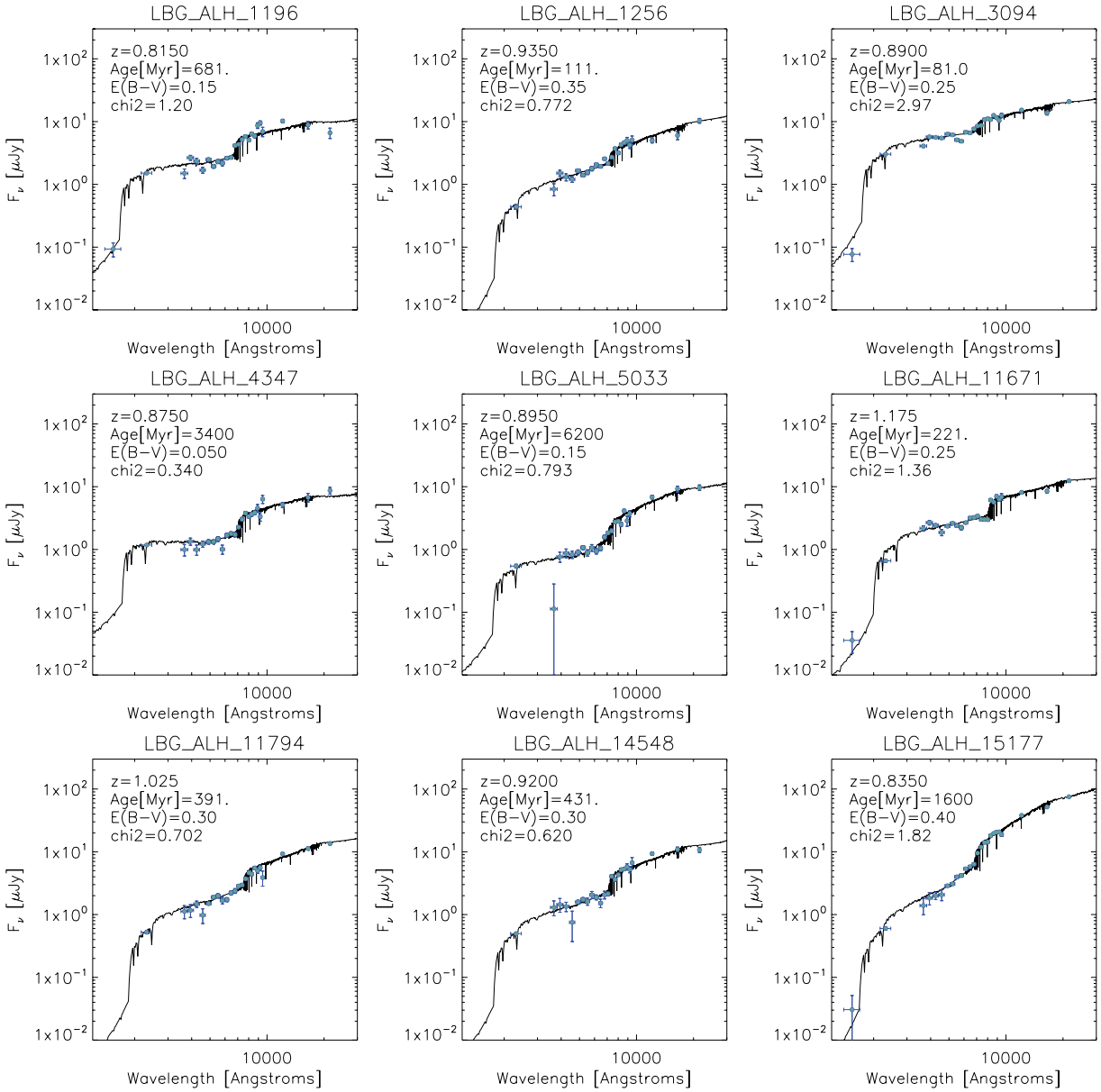

Figure 1. Examples of SED-fitting results with *GALEX*+ALHAMBRA data for nine *GALEX*-selected LBGs randomly selected from the whole sample. The blue points are the observed *GALEX* and ALHAMBRA fluxes, and the black curves are the best-fitting Bruzual & Charlot (2003) (BC03) templates of each object. The BC03 templates were build by assuming a constant SFR, a Salpeter IMF, and a fixed metallicity of $Z = 0.2\,Z_{\odot}$. In each panel we indicate the SED-derived redshift, age, dust attenuation, and reduced χ^2 associated with each best-fitting template. It can be seen that the combination of *GALEX* and ALHAMBRA data provides a very good sampling of the rest-frame UV continuum and the 4000-Å Balmer break of our UV-selected galaxies.

GALEX data is expected to give accurate determination of photometric redshifts ($z_{\rm phot}$) at the expected redshift range of *GALEX*-selected LBGs, namely $z \sim 1$. This is because at $z \sim 1$, *GALEX*+ALHAMBRA data cover the rest-frame UV continuum and the Balmer break, which are two of the most important features to fit in the SED of galaxies for determining photometric redshifts. In Fig. 3 we compare the obtained $z_{\rm phot}$ with spectroscopic redshifts ($z_{\rm spec}$) for those sources in the whole sample of 35 810 UV-selected galaxies with $\chi^2_{\rm r} < 10$ that have available spectra from the zCOSMOS survey (Lilly et al. 2007). Here we define the accuracy of $z_{\rm phot}$ as $\sigma_{\Delta z} = \Delta z/(1 + z_{\rm spec})$, with $\Delta z = |z_{\rm phot} - z_{\rm spec}|$. See also Matute et al. (2012) for a discussion of the photometric redshift accuracy of the ALHAMBRA survey. It can be seen in Fig. 3 that within the redshift range $0.8 \lesssim z \lesssim 1.2$ there is a good agreement between the photometric and spectroscopic redshifts, namely $\sigma_{\Delta z}$ less than 0.05 for most galaxies (see the horizontal dashed lines). It should be noted that this accuracy applies only to galaxies that are as bright as the sources in the spectroscopic survey. All the galaxies with spectroscopic redshift from the zCOSMOS survey shown in Fig. 3 have *r*-band observed magnitudes typically brighter than 23.5 mag, and therefore the reliability of the photometric redshifts can be guaranteed up to that limit. Hereafter, photometric redshifts are used for the sources without a zCOSMOS counterpart. For those sources with a zCOSMOS spectrum, we redo the SED fits and employ the results based on $z_{\rm spec}$.

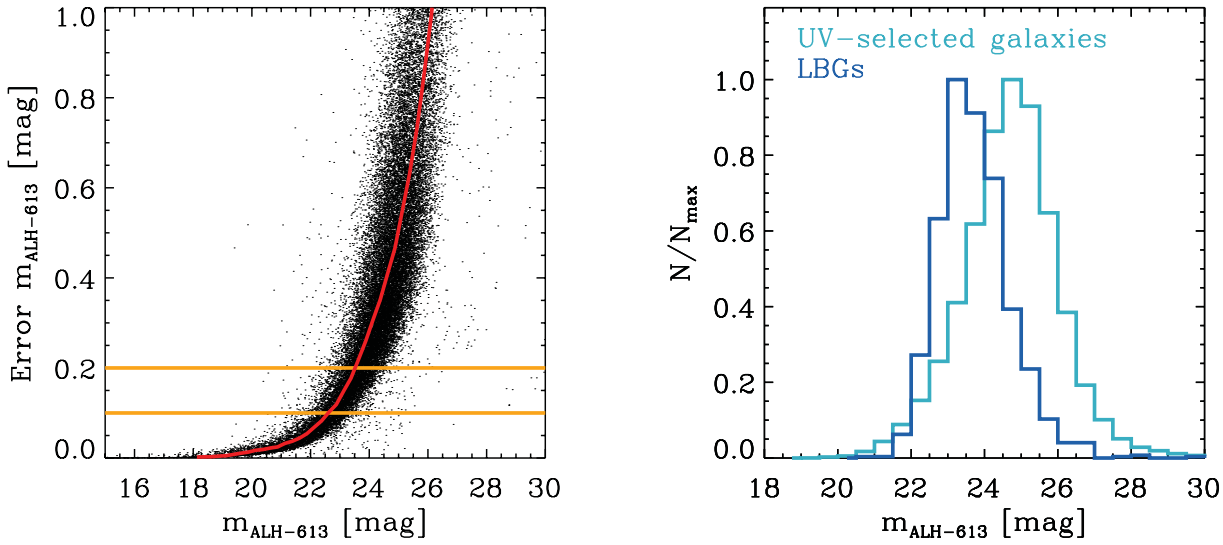

Figure 2. Left: Photometric errors against the observed magnitude in the ALHAMBRA filter centred at 613 nm for our sample of UV-selected galaxies with ALHAMBRA measurements and $\chi^2_r < 10$ in the SED-fitting results. The red curve corresponds to the median value of the error distribution for each value of the observed magnitude. Horizontal lines represent photometric errors of 0.1 and 0.2 mag. Right: Distribution of the observed magnitude in the ALHAMBRA filter centred at 613 nm for LBGs and a sample of UV-selected galaxies with ALHAMBRA counterparts at the same redshift range as LBGs. Histograms have been normalized to their maxima in order to clarify the representation.

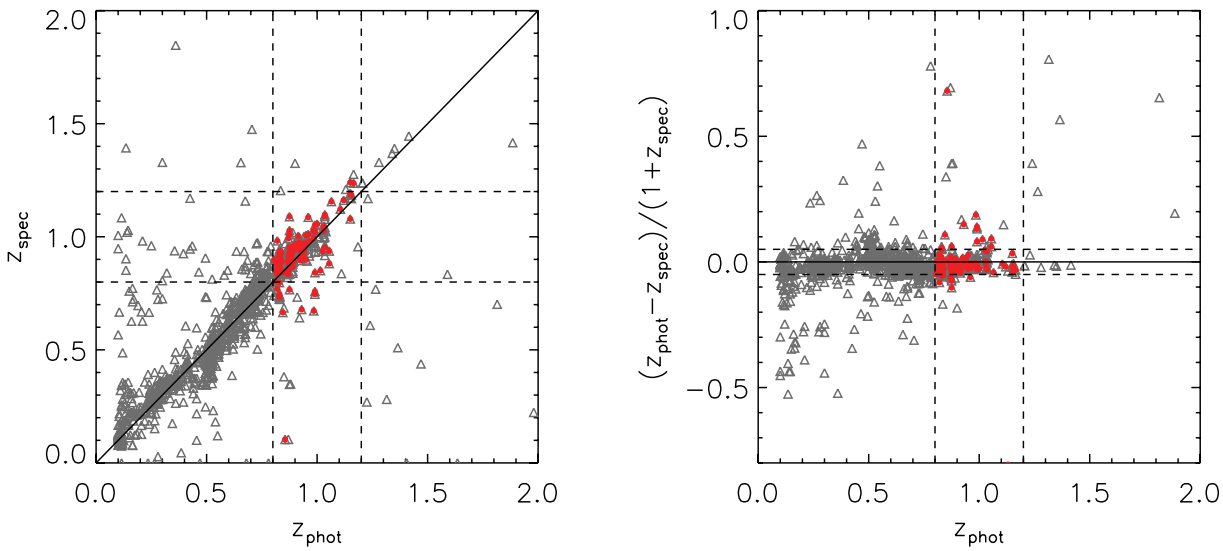

Figure 3. Accuracy of the photometric redshift determination with the combination of *GALEX* and ALHAMBRA data for the whole sample of 35 810 UV-selected galaxies with ALHAMBRA measurements and $\chi^2_r < 10$ in the SED-fitting results. In these plots, only galaxies with available spectroscopic redshift from the zCOSMOS survey (Lilly et al. 2007) are considered. Red dots represent our *GALEX*-selected LBGs, and grey open triangles are the remaining galaxies in the sample. In the left panel, the vertical and horizontal dashed straight lines represent the photometric redshift locus where most *GALEX*-selected LBGs are expected to be located according to their UV colour selection, $0.8 \lesssim z \lesssim 1.2$. In the right panel, the vertical dashed straight lines represent the photometric redshift locus where most *GALEX*-selected LBGs are expected to be located according to their UV colour selection. The horizontal dashed straight lines indicate the values of the photometric redshift accuracy, $\sigma_{\Delta z} = \Delta z/(1 + z_{spec})$, equal to ± 0.05. The horizontal continuous straight line represents where spectroscopic and photometric redshifts would agree.

4 UV-SELECTED GALAXIES AT $z \sim 1$

As noted in Section 1, the choice of the red-ward and blue-ward filters determines the wavelength at which the Lyman break is located and, therefore, the redshifts of the selected galaxies. In this work we aim to analyse the physical properties of those LBGs whose Lyman break is located between the *GALEX* FUV and NUV filters, which are centred at 1528 and 2271 Å (in terms of their effective wavelengths) and have bandwidths of 1344–1786 and 1771–2831 Å, respectively. These wavelengths imply that the redshifts of these *GALEX*-selected LBGs are expected to be around $z \sim 0.95$ considering an intermediate wavelength of 1780 Å between the two filters.

In order to formulate an analytic selection criterion to segregate our LBGs we use a large set of BC03 templates associated with a metallicity of $Z = 0.2\,Z_\odot$, a constant SFR, and various values of age and dust attenuation. We study the location of those templates in a colour–colour diagram as a function of redshift. To do that, each

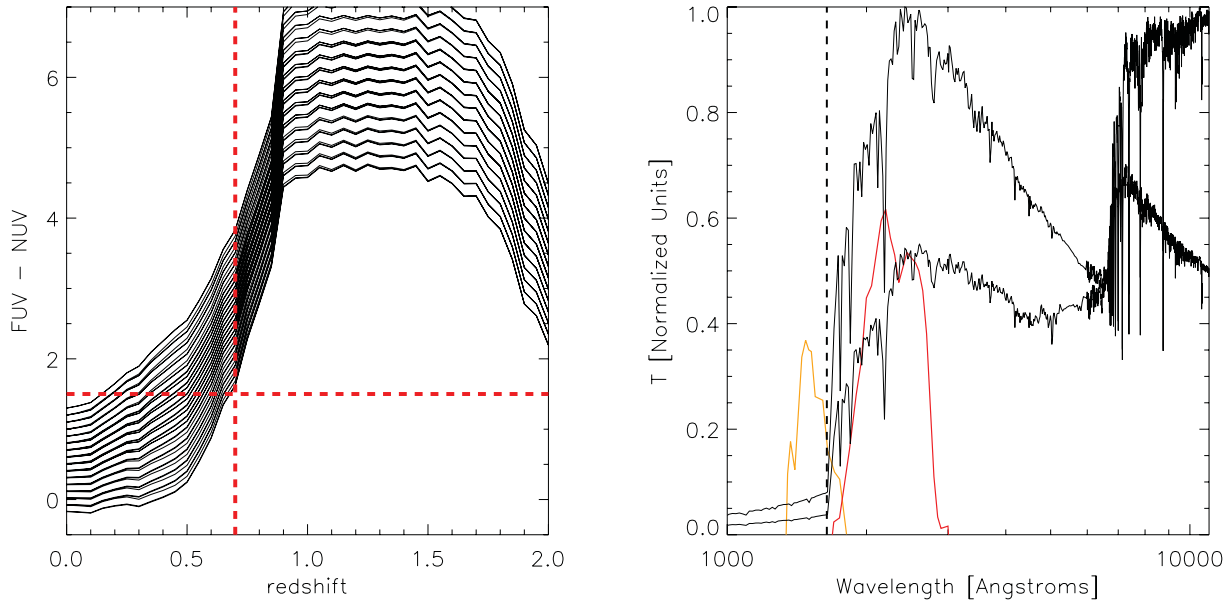

Figure 4. Colour selection of the *GALEX*-selected LBGs studied in this work. Left: synthetic FUV–NUV colour tracks as a function of redshift according to a set of Bruzual & Charlot (2003) (BC03) stellar population templates associated with different values of age and dust attenuation. The horizontal dashed red line indicates the colour cut employed in this work, which, according to the tracks shown in black, is expected to select galaxies at $z \geq 0.7$ (vertical red dashed line). Right: Transmission curves of the FUV (orange) and NUV (red) *GALEX* filters. We also show the location of the Lyman break at $z = 0.8$ with a vertical dashed black line and the BC03 stellar population templates associated with two different values of age and dust attenuation (black curves). It can be seen that, although the colour selection shown in the left panel is expected to segregate galaxies at $z \geq 0.7$, the Lyman break does not almost completely pass the FUV channel until $z \sim 0.8$.

template is redshifted from $z = 0$ up to $z = 2$, and then we apply the corresponding absorption in the intergalactic medium following the Madau et al. (1996) prescription, and obtain the $FUV - NUV$ synthetic observed colours by convolving the templates with the transmission curves of the *GALEX* filters. The results are shown in Fig. 4. As a general trend and as could be expected by the location of the Lyman break as a function of redshift, the $FUV - NUV$ colour increases with redshift up to $z \sim 1$. Looking at the different tracks represented in Fig. 4, we decided to impose a colour cut of 1.5 (red dashed horizontal line), and therefore our colour selection for *GALEX*-selected LBGs is

$$FUV - NUV > 1.5. \quad (2)$$

It is important to note that the application of this criterion requires the detection of each galaxy in both the FUV and the NUV channel. The left panel of Fig. 4 indicates that in imposing such a colour selection criterion we segregate galaxies located at $z \geq 0.7$ (this threshold is represented by the red dashed vertical line). At $0.7 \leq z \leq 0.8$, however, the FUV flux is strongly affected by the photons of the Lyman continuum (Lyc); that is, by those UV photons whose wavelengths are lower than the wavelength of the Lyman break. Therefore, if we really want to sample the Lyman break between the FUV and NUV without a significant contamination of Lyc photons in the FUV filter we have to limit the redshift of the galaxies to $z \geq 0.8$. This situation is schematized in the right panel of Fig. 4. Thus, we define, as a first approximation, *GALEX*-selected LBGs as those galaxies that are detected in both the FUV and the NUV channel and whose fluxes in each band satisfy equation (2) and are located at $z \geq 0.8$. This sample comprises 475 galaxies.

It is worth noting that there is a difference between the selection criterion that we apply here and those applied to look for high-redshift LBGs. At $z \gtrsim 2$, LBGs are usually found by employing not only the difference in colour that characterizes the Lyman break (equation 2) but also a difference in colour at redder wavelengths (see for example Steidel et al. 2003; Madau et al. 1996). This is done in order to rule out lower-redshift interlopers. This is important because at high redshifts the photometric redshifts might suffer from large uncertainties, and then it is not always possible to select galaxies in a specific redshift range based on $z_{\rm phot}$. However, in our case, as noted in Section 3.1 and shown in Fig. 3, we have accurate values of the photometric redshift for our UV-selected galaxies at $z \sim 1$, and therefore that supplementary condition is not needed. Barger, Cowie & Wang (2008) selected LBGs at $0.6 \leq z \leq 1.4$ by employing a double colour selection criterion combining $FUV - NUV$ and $NUV - U$. If we limit our sample in NUV magnitude to their limit, $NUV < 23.75$, all but one of our *GALEX*-selected LBGs satisfy the double colour selection criterion of Barger et al. (2008). This is schematized in Fig. 5. The U-band data for the galaxies in the panel have been taken from the broad-band photometric catalogue in the COSMOS field (Capak et al. 2007). Conversely, if we trust the photometric redshifts obtained from the combination of *GALEX* and ALHAMBRA data we find that with the selection criterion of Barger et al. (2008) we would miss a population of *GALEX*-selected LBGs fainter than $NUV = 23.5$ mag whose $NUV - U$ colour is typically redder than those of *GALEX*-selected LBGs with $NUV < 23.5$ mag.

The application of equation (2) requires the detection of the galaxies in both the FUV and the NUV *GALEX* channels so that the amplitude of the break can be measured. However, it is possible that a galaxy has such a strong Lyman break that is is detected in the NUV but undetected in the FUV channel. In order to include these FUV-undetected galaxies in the sample of *GALEX*-selected LBGs we have to ensure that the non-detection in FUV is caused by a strong Lyman break. FUV observations in the COSMOS field have a limiting magnitude of $FUV \sim 26.5$ mag. Galaxies brighter than that value in the wavelength range covered by the FUV filters

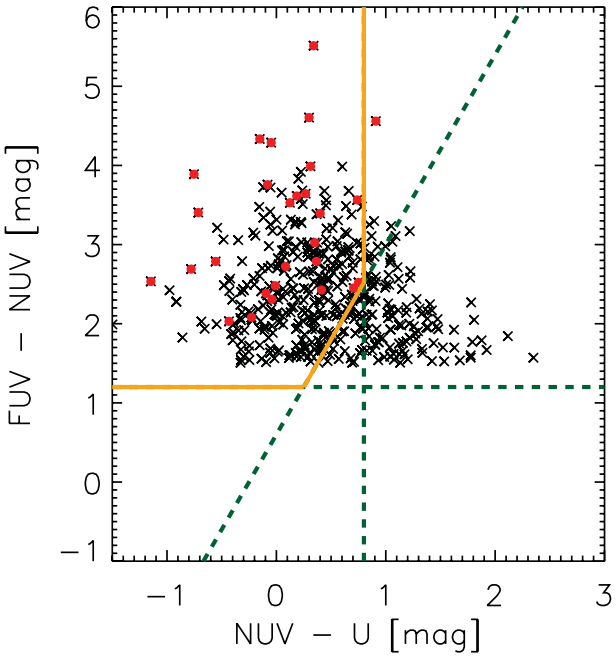

Figure 5. Location of our *GALEX*-selected LBGs in a colour–colour diagram. The window enclosed by the orange solid lines is the selection region for LBGs at $0.6 < z < 1.4$ with $NUV < 23.75$. The subsample of our *GALEX*-selected LBGs that satisfy $NUV < 23.75$ are represented with red filled dots, while the remaining fainter LGBs are plotted with black symbols.

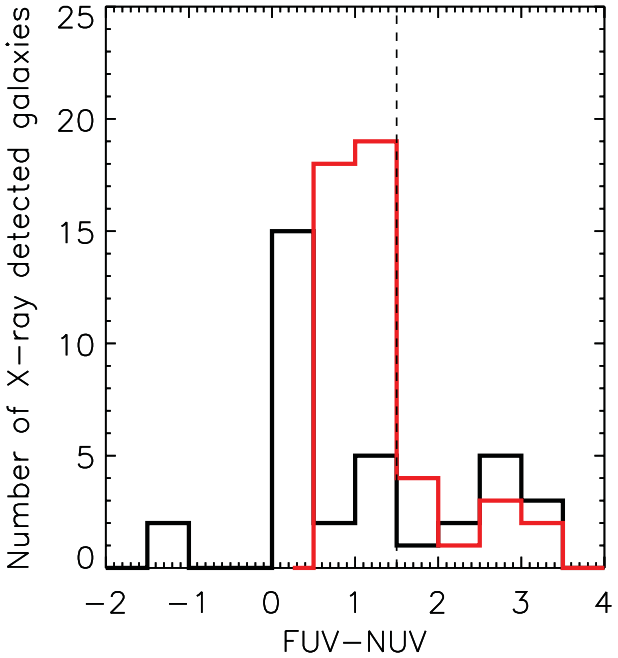

Figure 6. Distribution of the $FUV - NUV$ colour for X-ray-detected galaxies at $0.8 \leq z \leq 1.2$ with *GALEX* and ALHAMBRA counterparts (black histogram). The red histogram represents the distribution of the $FUV - NUV$ colour of the galaxies at $0.8 \leq z \leq 1.2$ spectroscopically classified as AGNs in Cowie, Barger & Hu (2010) via emission-line diagnosis. The vertical dashed line indicates the colour threshold for selecting LBGs in this work. In this plot, only galaxies with detection in both the *FUV* and the *NUV* channel are included.

should have been detected. Because we select LBGs with a $FUV - NUV$ colour cut of 1.5, that limiting magnitude would imply a limit of 25 mag in the NUV channel. In this way, we include in the previous sample of LBGs those galaxies that are brighter than 25 mag in the NUV channel, are at $0.8 \leq z \leq 1.2$, and are undetected in the FUV channel. This method for selecting FUV-undetected LBGs has also been applied in, for example, Burgarella et al. (2007). With these galaxies included, we end up with an initial sample of 1246 *GALEX*-selected LBGs. A visual inspection of the galaxies with available ACS information (see Section 6 for more details) reveals that the contamination due to the low spatial resolution of the *GALEX* images is lower than 5 per cent. In addition, from this visual inspection we check that there is no stellar contamination in the derived LBG sample.

4.1 X-ray counterparts and AGN contamination

In this work we are interested only in those LBGs that are SF galaxies, and we therefore need to rule out the active galactic nucleus (AGN) contribution. With this aim, we look for *Chandra* X-ray detections (Elvis et al. 2009) around 3 arcsec (Pović et al. 2009, 2012) of the ALHAMBRA-based spatial coordinates of our *GALEX*-selected LBGs. The area where our LBGs are located is almost totally covered by the *Chandra* footprint. We find that only 21 LBGs are detected in the X-ray and, therefore, probably have an AGN nature. When using the catalogue of AGNs in the COSMOS field (Salvato et al. 2011) we do not find any extra AGN identification. The only AGN-LBGs represent an AGN contamination of about 2 per cent.

Fig. 6 represents (black histogram) the distribution of $FUV - NUV$ colours of the galaxies in the whole sample of UV-selected sources with measurements in the FUV and NUV channels that are detected in the X-ray, have *GALEX* and ALHAMBRA counterparts, and are at $0.8 \leq z_{\rm phot} \leq 1.2$ (the redshift range within which our *GALEX*-selected LBGs are located). It can be seen that most X-ray-detected galaxies, and therefore galaxies with an AGN nature, have $FUV - NUV$ colours below the colour threshold utilized in this work for selecting LBGs (see equation 2). This UV colour distribution for AGNs at $z \sim 1$ explains the low percentage of AGNs among the *GALEX*-selected LBGs. We also plot in Fig. 6 the $FUV - NUV$ colour distribution of the galaxies spectroscopically classified as AGNs via emission-line diagnosis in Cowie et al. (2010) and which are located in the same redshift range as our *GALEX*-selected LBGs. It can be seen again that most AGNs at $z \sim 1$ have $FUV - NUV$ colours below the colour threshold considered in this work for selecting LBGs, reinforcing the fact that the LBG colour selection does not tend to segregate galaxies with an AGN nature.

Low values of the AGN contribution in samples of LBGs at different redshifts have also been reported. Lehmer et al. (2005) found AGN fractions of 1.2, 0.4, 0.3 and 0.4 per cent in their sample of U-, B_{435}-, V_{606}- and i_{775}-dropouts, respectively. Basu-Zych et al. (2011) reported an AGN fraction for their sample of LBGs at $0.5 < z < 2.0$ of 5–6 per cent, and Nandra et al. (2002) found an AGN contribution of about 3 per cent in their sample of LBGs at $z \sim 3$. In the subsequent analysis we do not take into consideration the *GALEX*-selected LBGs with an AGN nature. We thus end up with a sample of 1225 SF *GALEX*-selected LBGs. This is the largest sample of LBGs studied at $z \sim 1$ to date. Fig. 1 shows the UV-to-NIR SEDs of nine of the *GALEX*-selected LBGs in our final sample. This small subsample is representative of the whole sample of LBGs. It can clearly be seen that the combination of *GALEX* and ALHAMBRA provides an excellent coverage of the rest-frame UV continuum, Balmer break, and NIR SEDs of these galaxies.

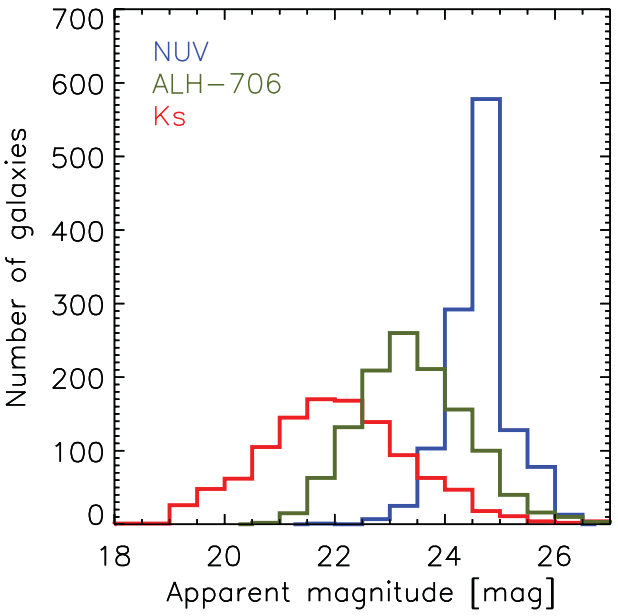

Figure 7. Distribution of the NUV (blue histogram), ALH-706 (green histogram), and *Ks* (red histogram) apparent magnitudes for our *GALEX*-selected LBGs at $z \sim 1$.

Fig. 7 represents the distributions of the apparent brightness of our *GALEX*-selected LBGs in the NUV channel, optical ALH-706 ALHAMBRA filter, and in the NIR *Ks* band. These distributions should be taken into account when comparing the results for our LBGs with those reported in other published studies that employ different photometric information. Our *GALEX*-selected LBGs at $z \sim 1$ have NUV magnitudes around 24.5–25.0 mag and optical magnitudes typically between 22 and 24.5 mag. The median value of their *Ks* magnitude is 22 mag. Furthermore, it can be seen that the spread in the magnitudes increases with the central wavelength of the filters. Whereas the NUV magnitudes are distributed mostly within a range of 1 mag width, the *Ks*-band magnitude spans from 20 to 24 mag.

4.2 High-redshift analogues

In this work, we also aim to compare the SED-derived physical properties of LBGs at different redshifts. LBGs at high redshift (i.e. $z > 3$) tend to be intrinsically more luminous than those selected in the present work owing to an observational bias. If we want to compare LBGs at different redshifts, and therefore galaxies that are selected with similar selection criteria, we must limit the rest-frame UV luminosity of our *GALEX*-selected LBGs at $z \sim 1$ to the same range as that for LBGs at $z > 3$, which is typically $\log(L_{\rm UV}/{\rm L}_{\odot}) \geq 10.2$. In this sense, we define *UV-bright LBGs* as those LBGs at $0.8 \lesssim z \lesssim 1.2$ that have $\log(L_{\rm UV}/{\rm L}_{\odot}) \geq 10.2$. This subsample is formed by 181 galaxies.

4.3 UV-faint galaxies

At the redshift range of our *GALEX*-selected LBGs there are many SF galaxies that are not selected through the dropout technique either because they do not have a strong break between the FUV and NUV filters or because they are undetected in the FUV channel and are not bright enough in the NUV filter to ensure a strong Lyman break between the two filters. All these galaxies will be termed *UV-faint galaxies*. This sample will not be studied in the present work but it will be used in a forthcoming work (Oteo et al. 2013b) in which FIR observations will be used to constrain the FIR SED of both *GALEX*-selected LBGs and UV-faint galaxies. In that case, the comparison between FIR-detected LBGs and UV-faint galaxies will help us to understand the galaxies that are selected under the dropout technique in opposition to other UV-fainter SF galaxies and to place LBGs in a more general scenario of SF galaxies at $0.8 \lesssim z \lesssim 1.2$.

5 SED-DERIVED STELLAR POPULATIONS

5.1 Physical properties of LBGs at $z \sim 1$

Fig. 8 shows with red shaded histograms the distributions of photometric/spectroscopic redshift, rest-frame UV luminosity, age, dust attenuation, dust-corrected total SFR, stellar mass, and UV continuum slope for our *GALEX*-selected LBGs. As a consequence of their selection criterion, our *GALEX*-selected LBGs are located at $0.8 \lesssim z \lesssim 1.2$ and have rest-frame UV luminosities $\log(L_{\rm UV}/{\rm L}_{\odot}) > 9.6$. The median values of the SED-derived physical properties of our *GALEX*-selected LBGs are summarized in Table 1. It can be seen that they are blue and young galaxies with moderate dust attenuation. Owing to their brightness in the rest-frame UV, they have relatively high values of the UV-derived and dust-corrected total SFRs.

In its maximum-likelihood mode, ZEBRA gives not only the best-fitting templates but also the probability that any of the other non-best-fitting templates can represent the photometric SED of a given galaxy. This probability can be used for deriving the uncertainties of the SED-derived parameters. With this aim, we define the weighted average (*WA*) of a given SED-derived physical property as $WA = \sum_i^N P_i f_i / N$, where P_i is the probability that a given template, i, can represent the observed SED of a given galaxy, f_i is the value of one of the physical properties associated with the ith template, and N is the number of templates. If the best-fitting template of a given galaxy has a much higher probability of representing its observed SED than any of the other templates, the average *WA* of a given physical property would be quite similar to the best-fitting one and the uncertainty of that property should be low. On the other hand, if several templates associated with very different values of a given property have a similar probability of representing the observed SED of a given galaxy, the *WA* would be dissimilar to the best-fitting value, and the uncertainty should be high. Following this idea, we define the uncertainty of a given parameter as the difference between the best-fitting value and its corresponding weighted average.

The physical parameters intrinsically related to the BC03 templates considered in this work are the age and the dust attenuation. The UV-derived dust-uncorrected SFR is obtained from the normalization of each observed template to the observed SED, and the stellar mass is obtained from the values of age, dust attenuation, and dust-uncorrected SFR. Thus, the procedure outlined above for deriving the uncertainties should be first applied to age and dust attenuation. As a result, we obtain that the median values of the uncertainties of age and dust attenuation for our LBGs are $\Delta{\rm Age} = 390$ Myr and $\Delta E_s(B-V) = 0.05$, respectively. The typical uncertainty of the SED-derived age is of the same order as the median age of our *GALEX*-selected LBGs. This implies that, even with the exceptional photometric coverage of the ALHAMBRA survey, which samples quite well the Balmer break of SF galaxies at $z \sim 1$, the age is a parameter difficult to determine accurately with an

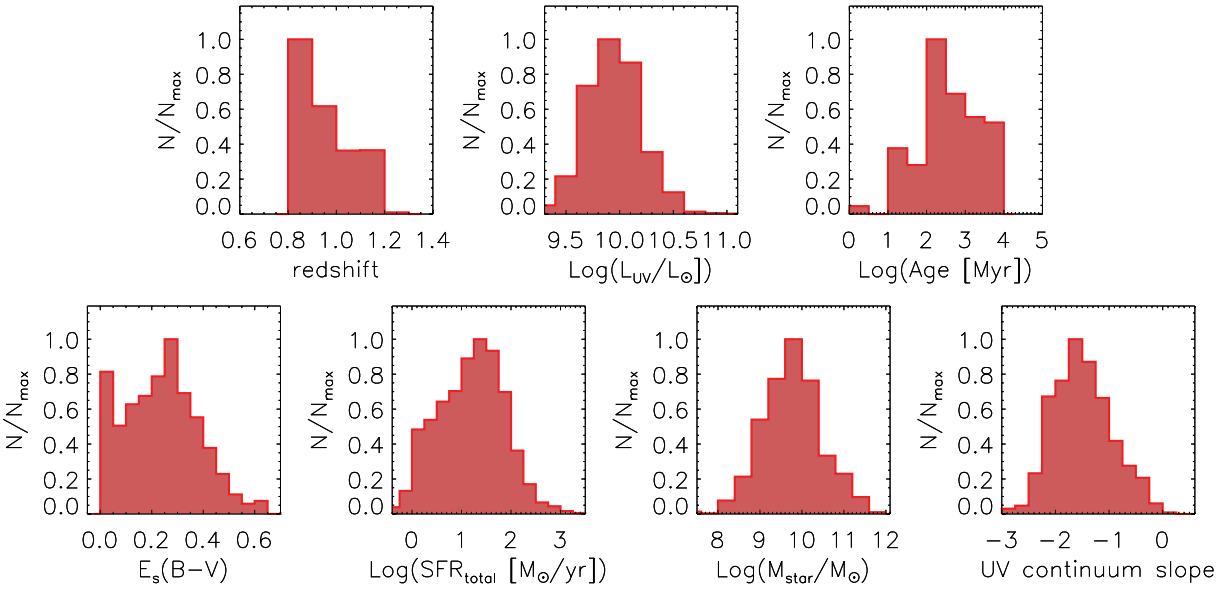

Figure 8. From left to right and from top to bottom, distributions of redshift (photometric or spectroscopic), rest-frame UV luminosity, and SED-derived age, dust attenuation, dust-corrected total SFR, stellar mass, and UV continuum slope for our *GALEX*-selected LBGs. Bruzual & Charlot (2003) (BC03) templates associated with a constant SFR, Salpeter IMF, and metallicity $Z = 0.2\,Z_{\odot}$ are considered in the SED fits. Histograms have been normalized to their maxima.

Table 1. SED-derived physical properties of the studied *GALEX*-selected LBGs at $z \sim 1$.

Property	Median value	Width of the distribution
Age [Myr]	341	2206
$E_s(B-V)$	0.20	0.14
$SFR_{\rm UV}$ [$M_{\odot}$ yr^{-1}]	1.90	2.63
$SFR_{\rm total}$ [$M_{\odot}$ yr^{-1}]	16.94	112.94
$\log(M_*/M_{\odot})$	9.74	0.75
UV slope	−1.53	0.55

SED-fitting procedure. The uncertainties in the SFR are directly related to the uncertainties of the rest-frame UV luminosity, and thus to the photometric uncertainties of the sources. The rest-frame 1500 Å is sampled by the NUV filter at $z \sim 1$. The typical uncertainty of the NUV magnitudes for the galaxies in our sample is 0.15. This value translates into a luminosity uncertainty of $\Delta \log(L_{\rm UV}/L_{\odot}) \sim 0.06$ and a UV-derived SFR uncertainty of $\Delta SFR = 0.15\,M_{\odot}$ yr^{-1}. Propagating the uncertainties of age, dust attenuation, and UV-derived SFR, we obtain typical uncertainties of 0.5 and 0.2 dex for $\log M_*/M_{\odot}$ and $\log SFR_{\rm total}$, respectively. The high uncertainty of the SED-derived stellar mass is a consequence of the fact that it comes from the combination of the uncertainties of age and dust attenuation. The uncertainties in the UV continuum slope are considered to be those obtained in the power-law fitting and turn out to have a median value of 0.15.

Nilsson et al. (2011) studied the optical SED-derived physical properties of a sample of 15 *GALEX*-selected LBGs at $z \sim 1$, taken from Burgarella et al. (2007), by fitting with BC03 templates their photometric points derived from ACS slit-less grism spectra. They obtained distributions for dust attenuation and stellar mass similar to those reported in the present work, but their ages tend to be lower. In their work, Nilsson et al. (2011) employed BC03 templates that are a combination of two single stellar populations (SSP) models, instead of the models with constant SFR assumed in the present work, and the ages reported are the youngest ones associated with the two SSP models used in the fittings. This is probably the reason why the age distribution of Nilsson et al. (2011) is shifted towards lower values. Basu-Zych et al. (2011) studied the physical properties of a sample of 50 LBGs at $0.5 < z < 2$ selected with the *Swift* ultraviolet/optical telescope. They reported lower values of stellar masses, $\langle \log M_*/M_{\odot} \rangle = 9.4 \pm 0.6$, than those obtained here and with a similar dust attenuation distribution. In this case, the differences are probably a result of the fact that their sample contains galaxies at higher redshifts than our LBGs, caused by the different red-ward and blue-ward filters adopted to segregate the galaxies.

5.2 Dependance on the assumed metallicity

In the elaboration of the BC03 templates employed to report the SED-derived physical properties of our *GALEX*-selected LBGs we adopted a fixed value of metallicity, $Z = 0.2\,Z_{\odot}$. In this section, we explore the differences in the SED-derived physical properties of the studied galaxies when considering BC03 templates associated with different values of metallicity. Furthermore, we analyse whether it is possible to constrain the metallicity of our studied galaxies with an SED-fitting procedure with the exceptional photometric coverage that the combination of *GALEX* and ALHAMBRA data provides. With this aim, we built five more sets of BC03 templates associated with the other metallicities available in the software GALAXEV and redid the SED fits. In this process, we assume the same IMF, IGM absorption and consider the same sampling in age and dust attenuation as in Section 3. We also employ a constant SFH. We then retain the values of $\chi^2_{\rm r}$, age, dust attenuation, and stellar mass obtained with the fits for the different metallicities. We first compare the ratios between the $\chi^2_{\rm r}$ associated with the SED-fitting results with a set of templates of different metallicities for individual galaxies (see Fig. 9). It can be seen that the ratios in the $\chi^2_{\rm r}$ are very close to unity, and consequently we cannot distinguish between different metallicities with our photometric SEDs built with *GALEX* and ALHAMBRA data. In order to examine the implications of this degeneracy in the SED-derived properties of our galaxies, we represent in Fig. 10 the median age, dust attenuation, stellar mass, and dust-corrected total SFR of our galaxies as a function of the

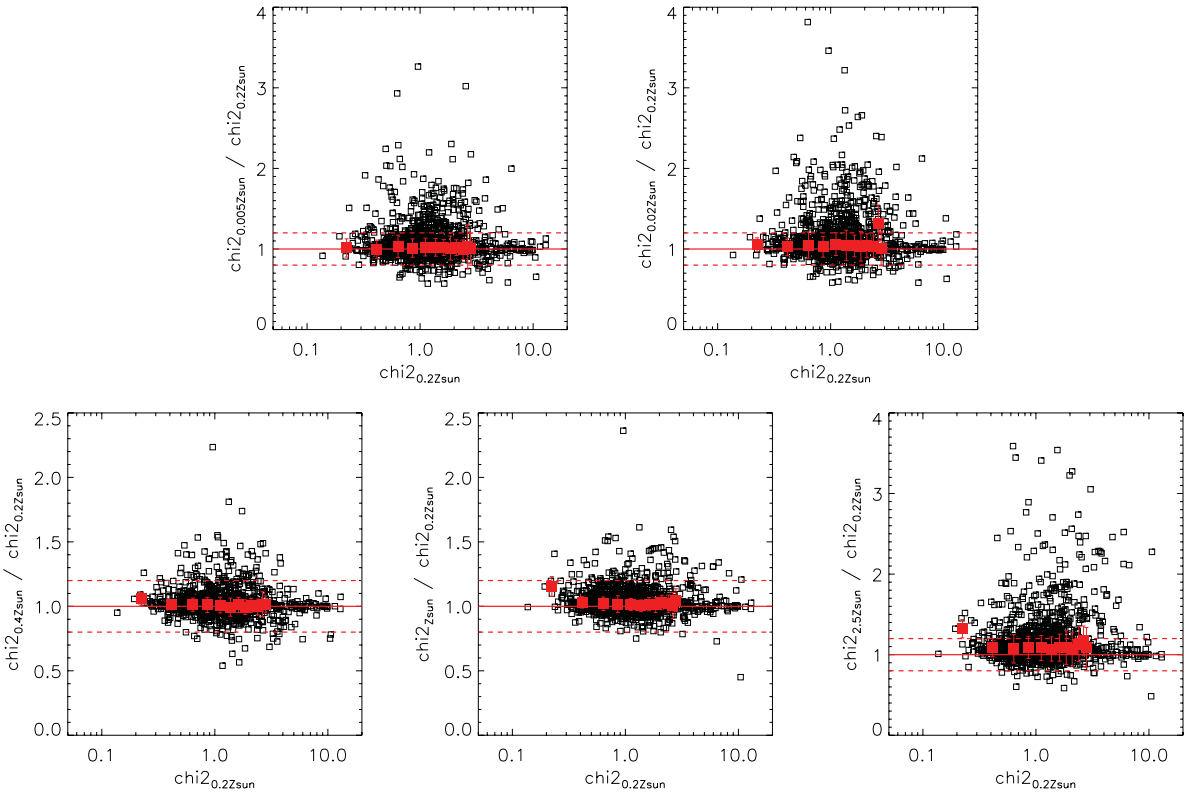

Figure 9. Relation between the χ^2_r values of the SED-fitting results with Bruzual & Charlot (2003) (BC03) templates built by assuming different metallicities. Red filled squares represent the the median χ^2_r ratios represented on the *y*-axis in different bins of the χ^2_r associated with SED-fitting results with metallicity $Z = 0.2\,Z_{\odot}$, the value adopted in this work for reporting the SED-derived properties of the studied galaxies. Red solid horizontal lines represent the one-to-one relation.

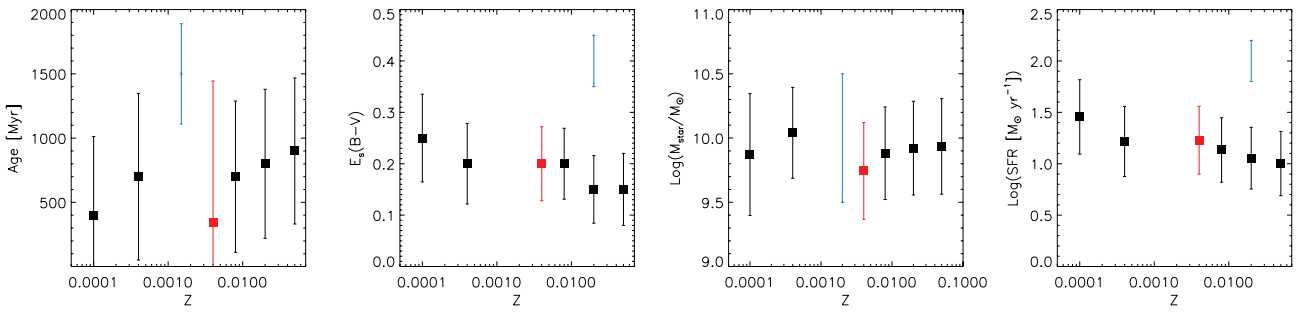

Figure 10. Differences in the SED-derived age, dust attenuation, stellar mass, and dust-corrected total SFR when assuming Bruzual & Charlot (2003) (BC03) templates associated with different metallicities. The dust-corrected total SFR is the one obtained by correcting the rest-frame UV luminosity with the SED-derived dust attenuation, $E_s(B-V)$. The squares represent the median values over the whole sample of *GALEX*-selected LBGs at $z \sim 1$ of each parameter for each value of the metallicity considered in the SED fits. The red symbols represent the results for the metallicity adopted in this work for reporting the SED-derived properties of our galaxies. Error bars indicate the width of the distributions of each parameter for each value of metallicity. The typical uncertainties associated with each parameter are shown with blue bars.

metallicity assumed in the SED fits. As can be seen, the differences in the SED-derived parameters are within their typical uncertainties for most cases. Because we cannot discriminate different values of metallicity, the difference between the median values shows the intrinsic uncertainties in the SED-fitting procedure.

5.3 Dependance on the assumed SFH

The physical properties of our *GALEX*-selected LBGs that were discussed in the previous section were derived by carrying out an SED-fitting procedure with BC03 templates built by assuming a constant SFR. Different works assume different SFHs for the galaxies under study (Nilsson et al. 2011; Basu-Zych et al. 2011; Haberzettl et al. 2012; Hathi et al. 2013). One of the most commonly used is that in which the SFH varies exponentially with time. Analytically, it can be described by $SFH \propto \exp(-t/\tau_{\rm SFH})$, where $\tau_{\rm SFH}$ is the SFH time-scale. It should be noted that the constant SFR is a particular case of the exponentially declining SFH when the SFH time-scale tends to infinity. The use of exponentially declining SFHs entails the fitting of the SFH time-scale, increasing the number of degrees of freedom. Furthermore, there is a degeneracy between the SED-derived age and the SFH time-scale that means that different combinations

of age and $\tau_{\rm SFH}$ give templates with the same shape that might be undistinguishable with photometric SEDs. In this section we analyse the differences in the SED-derived physical properties for our *GALEX*-selected LBGs when assuming SFHs with different values of the SFH time-scale. Furthermore, we analyse whether we can distinguish between different values of $\tau_{\rm SFH}$ and, therefore, constrain the SFH of our galaxies

We build another set of BC03 templates considering that the SFH varies exponentially with time, with values $\tau_{\rm SFH} = 0.0001$, 0.001, 0.01, 0.1, 1, 2, 5, 10 and 50 Gyr. In this process we adopt again a Salpeter (1955) IMF, distributing stars from 0.1 to 100 $M_\odot$, and select a fixed value of $Z = 0.2\,Z_\odot$ for the metallicity. We select the same values of dust attenuation, $E_s(B-V)$ and age as adopted in Section 3. We also include IGM absorption, adopting the prescription of Madau (1995). Figs 11, 12 and 13 show the differences found for the SED-derived age, stellar mass, and dust attenuation, respectively, when assuming different SFHs. In these plots, the colour code indicates the ratio of the $\chi^2_{\rm r}$ values between the SED-fitting results with a given $\tau_{\rm SFH}$ and the case of constant SFR. In those cases for which that ratio is close to one, the SED-fitting procedure would not be able to discriminate between different kinds of SFHs. Regarding age, Fig. 11 indicates that, as expected, there is a degeneracy between age and $\tau_{\rm SFH}$. The SED-derived ages are systematically younger when adopting lower values of $\tau_{\rm SFH}$. This tendency is more significant for galaxies whose SED-derived ages with constant SFR are higher. For $\tau_{\rm SFH} \geq 1$ Gyr, the ratios of the $\chi^2_{\rm r}$ values obtained with different SFHs are very similar to unity, and therefore, although the SED-derived ages are different for different values of $\tau_{\rm SFH}$ (mostly for the oldest galaxies), the SED-fitting procedure is not able to distinguish between these SFHs. This produces an uncertainty in the age of the galaxies and prevents us from distinguishing between different temporal variations of their SFH. The ages derived with templates associated with constant SFH are typically higher than those obtained with templates of finite values of $\tau_{\rm SFH}$. In this way, the ages derived in Section 5.1 for our *GALEX*-selected LBGs might be considered as upper values.

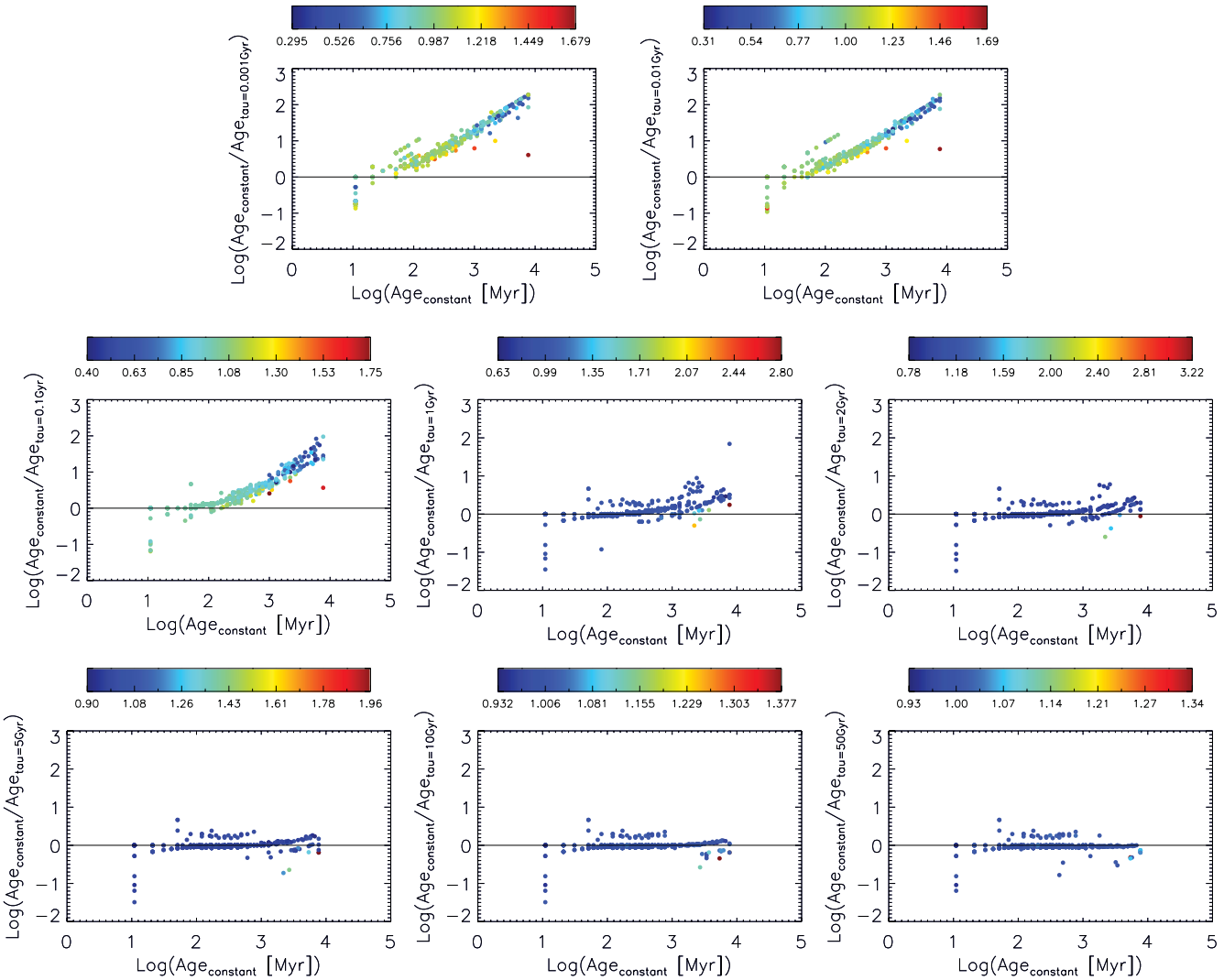

Figure 11. Differences between the SED-derived age when performing SED fittings with Bruzual & Charlot (2003) (BC03) templates associated with constant SFR and with BC03 templates associated with exponentially declining SFHs with finite values of the SFH time-scale. The colours of the points in each figure are related to the ratio in the $\chi^2_{\rm r}$ values between the SED-fitting results when considering the different kinds of SFHs. The values of such $\chi^2_{\rm r}$ ratios corresponding to each colour are indicated by the colour bars. Values close to one indicate that the templates associated with different SFHs fit the photometry with the same accuracy, and therefore it is not possible to distinguish between different kinds of SFHs. Each panel is associated with one value of the SFH time-scale, as indicated on each vertical axis.

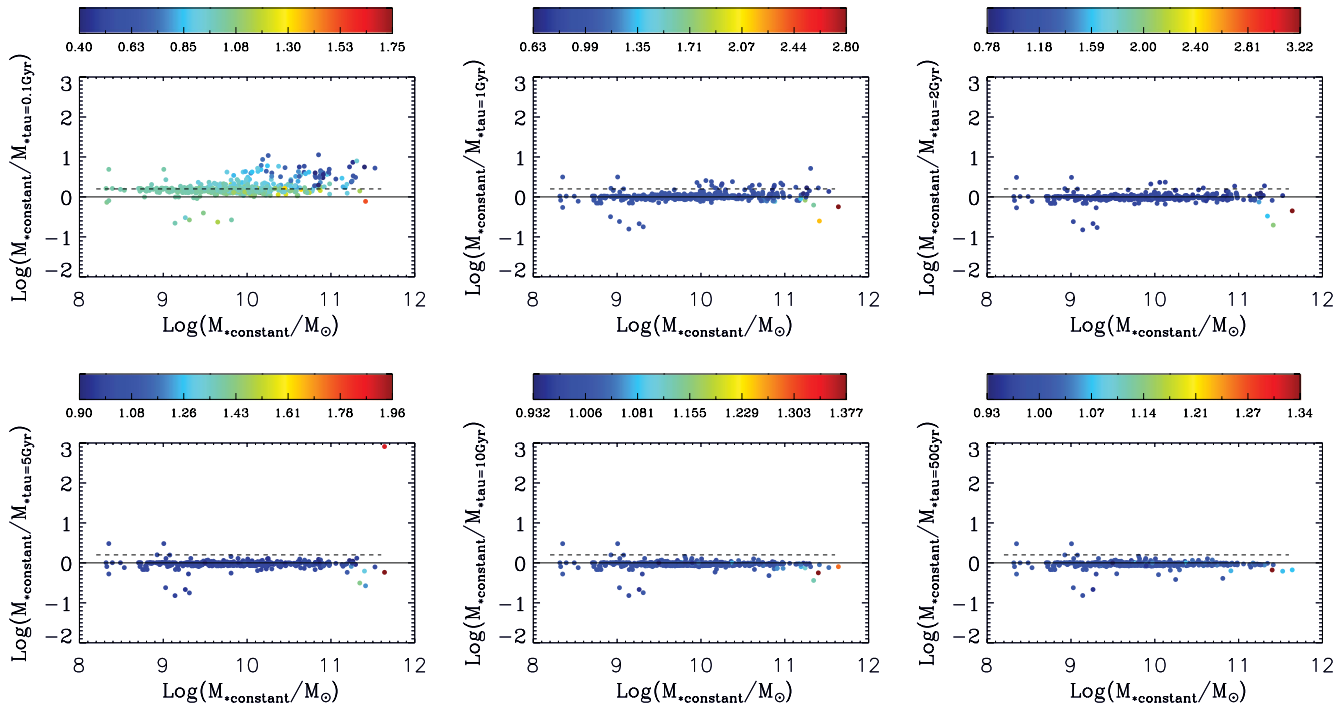

Figure 12. Differences between the SED-derived stellar mass when performing SED fittings with Bruzual & Charlot (2003) (BC03) templates associated with constant SFR and with BC03 templates associated with an exponentially declining SFH with finite values of the SFH time-scale. The colours of the points in each figure are related to the ratio in the χ^2_r values between the SED-fitting results when considering the different kinds of SFHs. The values of such χ^2_r ratios corresponding to each colour are indicated by the colour bars. Values close to one indicate that the templates associated with different SFHs fit the photometry with the same accuracy, and therefore it is not possible to distinguish between different kinds of SFHs. Each panel is associated with one value of the SFH time-scale, as indicated on each vertical axis.

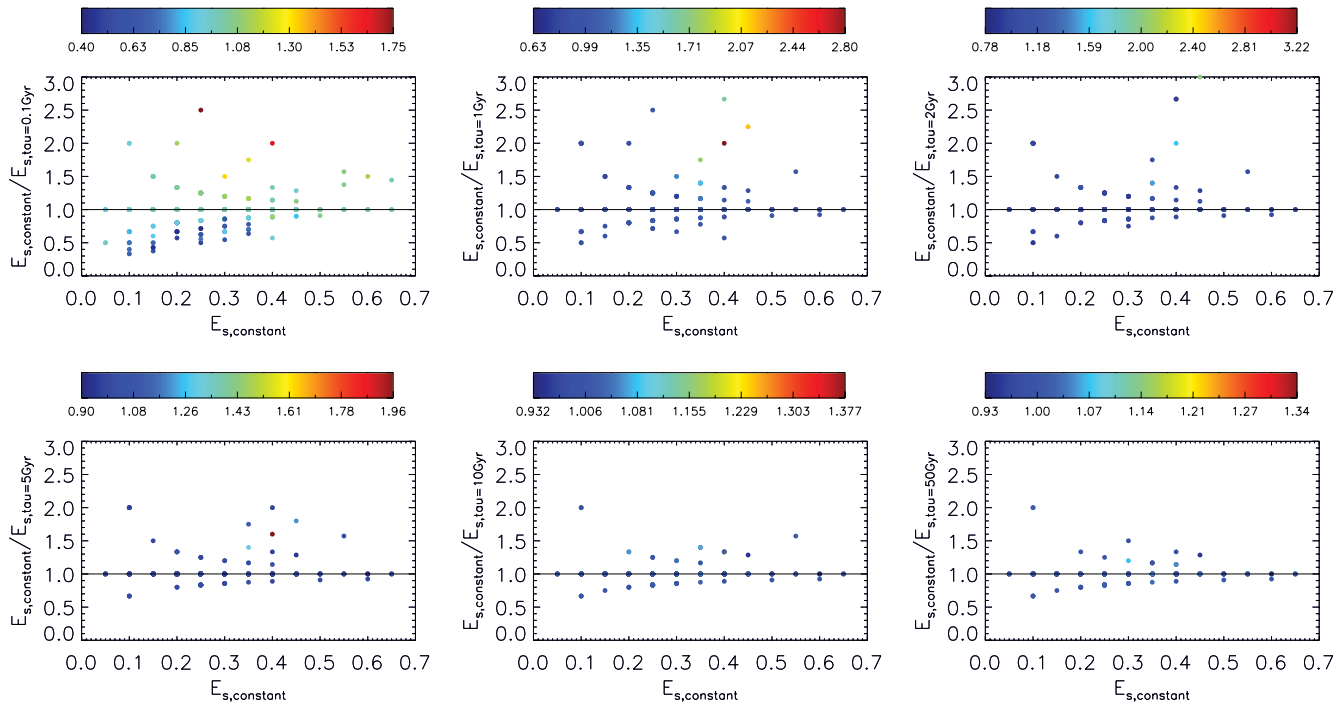

Figure 13. Differences between the SED-derived dust attenuation when performing SED fittings with Bruzual & Charlot (2003) (BC03) templates associated with a constant SFR and with BC03 templates associated with an exponentially declining SFH with finite values of the SFH time-scale. The colours of the points in each figure are related to the ratio in the χ^2_r values between the SED-fitting results when considering the different kinds of SFHs. The values of such χ^2_r ratios corresponding to each colour are indicated by the colour bars. Values close to one indicate that the templates associated with different SFHs fit the photometry with the same accuracy, and therefore it is not possible to distinguish between different kinds of SFHs. Each panel is associated with one value of the SFH time-scale, as indicated on each vertical axis.

Considering diverse SFH scenarios, the differences in age found are typically comparable to and in some cases higher (mostly for the lowest values of $\tau_{\rm SFH}$) than the typical uncertainty of the SED-derived age found in Section 5.1. Therefore, both the uncertainties in the SED-fitting procedure and the degeneracy between age and SFH affect the total uncertainty of the SED-derived age of our galaxies.

For $\tau_{\rm SFH} < 1$ Gyr, the ratio between the $\chi^2_{\rm r}$ values is similar to one for the majority of galaxies, but there is a population of them (those for which the age derived with constant SFR is higher) whose $\chi^2_{\rm r}$ values indicate that the templates associated with an exponential variation of the SFH are worse fitting. Only in these cases are we able to distinguish between different kinds of SFHs and, thus, as a general trend, we obtained that the SEDs of our oldest *GALEX*-selected LBGs are better fitted with BC03 templates associated with SFHs with $\tau_{\rm SFH} \geq 1$ Gyr, including the case of constant SFR.

Fig. 12 indicates that templates with lower values of $\tau_{\rm SFH}$ tend to give lower values of the stellar mass than those associated with higher values of $\tau_{\rm SFH}$. In this way, the stellar masses derived with constant SFR and reported in the previous section for our *GALEX*-selected LBGs might be understood as upper limits. Again, as is the case for age, even with the good photometric coverage of *GALEX* and ALHAMBRA we are not able to distinguish between the different SFH scenarios in most cases. In Fig. 12 the horizontal dashed line in each panel corresponds to a deviation of 0.2 dex with respect to the case of constant SFR. This is the maximum median difference that we find and it is a measurement of the uncertainty of the SED-derived stellar mass when considering various values of $\tau_{\rm SFH}$.

Fig. 13 shows that there is also a degeneracy between the SED-derived dust attenuation and the SFH time-scale. In this case, the tendency between dust attenuation and $\tau_{\rm SFH}$ is not as clear as those for age and stellar mass. The differences between the results with constant SFR and finite values of $\tau_{\rm SFH}$ are within a factor of two, although for most galaxies the two estimations agree.

Summarizing, even with the good photometric coverage of the combination of *GALEX* and ALHAMBRA data we are not able to distinguish between different SFHs for most cases. We can only conclude that older galaxies (in terms of the SED-derived age with templates associated with constant SFR) are better fitted with templates associated with $\tau_{\rm SFH} \geq 1$ Gyr. The differences between the SED-derived properties when assuming different kinds of SFHs imply additional uncertainties in the SED-derived parameters to those studied in Section 5.1.

5.4 SFR–stellar mass plane

One important parameter in the study of the physical properties of galaxies and their evolution is the specific star formation rate (sSFR). This quantity is defined as the ratio between the SFR and the stellar mass, sSFR = SFR/M_*, and it is a measurement of the present over past star formation activity. A tight relation between the SFR and the stellar mass has been found at different redshifts in several works (Salim et al. 2007; Elbaz et al. 2007; Noeske et al. 2007; Daddi et al. 2007; Pannella et al. 2009; Rodighiero et al. 2010; González et al. 2010; Karim et al. 2011; Elbaz et al. 2011). This has enabled the definition of a 'main sequence' (MS) of galaxies defined by a specific value of the sSFR. Galaxies in the MS are opposite to the idea of 'starburst galaxies', which are those galaxies whose nature makes them deviate from the MS towards higher values of the sSFR. The characteristic value of the sSFR for the MS of galaxies has been reported to change with redshift (see, for example, Elbaz et al. 2011 for a recent discussion of this evolution with deep *Herschel* FIR data). Previous studies show that the sSFR increases with increasing redshift at all masses and that the sSFR of massive galaxies is lower than that for less massive galaxies at any redshift (Feulner et al. 2005; Erb et al. 2006; Dunne et al. 2009; Damen et al. 2009; Rodighiero et al. 2010). Despite the number of studies analysing the relation between stellar mass and SFR, there is still some controversy, mostly regarding the slope of the sSFR–M_* relation.

In the left panel of Fig. 14 we show the dust-corrected total SFR for our *GALEX*-selected LBGs against their stellar mass. Along with the data points, the MSs of galaxies at $z \sim 1$ taken from Elbaz et al. (2007, 2011), and Noeske et al. (2007) are also represented. In that plot, red symbols indicate the dust-corrected total SFR obtained following the procedure explained in Section 3. Some other works recover the dust attenuation of galaxies by employing the UV continuum slope and a relation between the UV continuum slope and dust attenuation, such as the Meurer et al. (1999) law. The values of dust attenuation obtained in this way can also be used for obtaining the dust-corrected total SFR. Recently, it has been found that the smaller *IUE* apertures employed in Meurer et al. (1999) may have missed about half of the light. Consequently, for a given UV continuum slope, the newly found dust attenuations are lower than those predicted by the Meurer et al. (1999) relation (Overzier et al. 2011; Takeuchi et al. 2012). Following these results, we obtain the dust-corrected total SFR by correcting the UV luminosities with the dust attenuation derived from the UV continuum slope of our galaxies after the application of the Overzier et al. (2011) and Takeuchi et al. (2012) relations. Among the relations presented in Overzier et al. (2011), we employ the one for their Lyman break analogues. The results are also shown in the left panel of Fig. 14. It can be seen that whatever dust-correction method is applied, there is a clear relation between SFR and mass in the sense that more massive LBGs have higher SFRs. We fitted linear relations to the points obtained with the three dust-correction methods. Table 2 summarizes the results. It can be seen that the slopes of the SFR–mass relation obtained with the three dust-correction methods are very similar and compatible within the uncertainties. The differences between the zero-points of the relations are due to the fact that, for a given stellar mass, the dust attenuation recovered by each method is slightly different.

The right panel of Fig. 14 shows the relation between the sSFR and the stellar mass of our *GALEX*-selected LBGs. Again, we represent the points associated with the dust-corrected total SFR obtained from the SED-derived dust attenuation and also those derived from the UV continuum slope and the Meurer et al. (1999) law. It can be seen that galaxies with larger masses tend to have lower values of the sSFR, independently of the dust-correction method employed. We fitted a relation to the data points for the three dust attenuation methods. The best-fitting slope and zero-points are also shown in Table 2. It can be seen that the slope of the sSFR–mass relations are very similar for the three dust-correction methods and compatible within the uncertainties. Again, the differences between the zero-points are due to the slightly different dust attenuation obtained for a given stellar mass in each of the dust-correction methods.

6 SIZES AND MORPHOLOGY

In this section we study the morphology and the physical sizes of our *GALEX*-selected LBGs. To this end, we use *I*-band ACS images taken from the *HST* observations of the COSMOS field, which for our redshift range correspond to a rest-frame band ranging from approximately 3500 to 4250 Å. Out of the whole sample of LBGs, 897 have ACS information. We downloaded 8 arcsec × 8 arcsec ACS

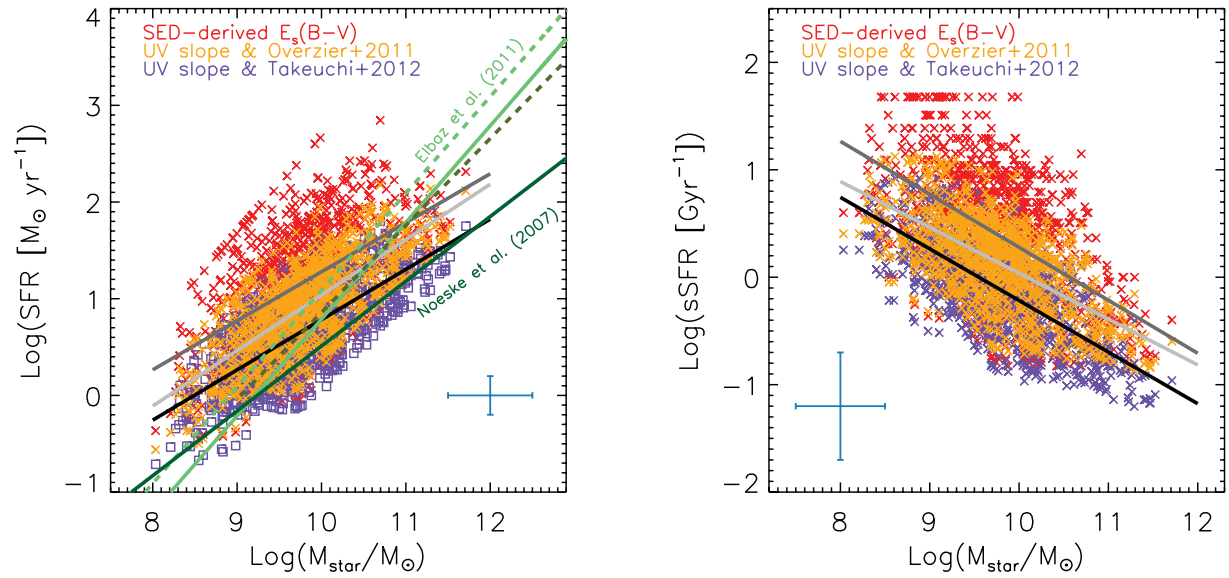

Figure 14. Left: Dust-corrected total SFR for our *GALEX*-selected LBGs as a function of their stellar mass. Red symbols correspond to the dust-corrected total SFRs obtained with the SED-derived dust attenuation (as explained in Section 3). Orange symbols represent the dust-corrected total SFRs obtained with the dust attenuation derived from the UV continuum slope using the Overzier et al. (2011) relation for Lyman break analogues. Purple symbols are obtained with the updated Meurer, Heckman & Calzetti (1999) relation given by Takeuchi et al. (2012) when correcting for the small aperture of *IUE*. The dark grey, light grey, and black straight lines are the linear fits to the red, orange, and purple symbols, respectively. For comparison, we also show the SFR–mass relations for the main sequence of galaxies at $z \sim 1$ reported in Elbaz et al. (2011) (light green solid line), Elbaz et al. (2007) (grey dashed line), and Noeske et al. (2007) (dark green solid line) at a similar redshift range as that for our *GALEX*-selected LBGs. The dashed light green line represents twice the value of the main sequence of Elbaz et al. (2011). Right: Specific SFR of our *GALEX*-selected LBGs as a function of their stellar mass. The meanings of the colours and the fits are the same as those in the left panel. In both plots, the error bars represent the typical uncertainties in the SED-derived total SFR, stellar mass, and sSFR (see Section 5.1). The uncertainty of the SED-derived total SFR corresponds to the values obtained when dust-correcting with the SED-derived dust attenuation.

Table 2. Results of a linear fitting to the SFR–mass and sSFR–mass relations for our *GALEX*-selected LBGs at $z \sim 1$. The data points are fitted to a relation in the form $\log SFR\,[\mathrm{M}_\odot\,\mathrm{yr}^{-1}] = a + b \log M_*/\mathrm{M}_\odot$ and $\log sSFR\,[\mathrm{Gyr}^{-1}] = a + b \log M_*/\mathrm{M}_\odot$. The results for the three dust-correction method described in the text are included.

SFR–mass	$E_s(B-V)$	Overzier et al. (2011)	Takeuchi et al. (2012)
a	-3.79 ± 0.25	-4.69 ± 0.16	-4.41 ± 0.15
b	0.50 ± 0.03	0.57 ± 0.02	0.51 ± 0.02
sSFR–mass	$E_s(B-V)$	Overzier et al. (2011)	Takeuchi et al. (2012)
a	5.21 ± 0.25	4.30 ± 0.16	4.59 ± 0.15
b	-0.49 ± 0.03	-0.42 ± 0.02	-0.48 ± 0.02

cutouts centred at the position of each source from the cutout service available from the NASA/IPAC Infrared Science Archive.[2] In order to study the morphology of the galaxies we carried out a visual inspection of each cutout and classified them into six groups, namely disc galaxies, compact galaxies, chain galaxies (CH), clump cluster (CC) galaxies, interacting/merging galaxies and irregular galaxies. For the definition of CH and CC we follow Elmegreen et al. (2009), and consider a galaxy as irregular when its morphology does not fit in any of the other groups. As a result of the visual classification, we found that the majority (69 per cent) of our *GALEX*-selected LBGs are disc-type galaxies, 11 per cent have indications of interactions or merging, 7 per cent are irregular, 6 per cent are compact galaxies, and a minority are CH or CC galaxies, with fractions of 5 and 2 per cent, respectively. It should be noted that a visual classification is always a very subjective procedure, and therefore the above percentages are approximate. However, what it is quite clear is that the dominant morphology of our *GALEX*-selected LBGs at $z \sim 1$ is the disc-like class. Wolf et al. (2005) studied the contribution to the UV luminosity density of different morphologies of galaxies at $z \sim 0.7$ by combining high-resolution images from the GEMS survey (Rix et al. 2004) with redshifts and SEDs from the COMBO-17 survey (Wolf, Meisenheimer & Röser 2001; Wolf et al. 2004). They reported that seemingly normal disc galaxies are the largest contributors to the UV luminosity density. This is compatible with the result that we find in the present work, as LBGs are among the brightest UV galaxies and most of them have disc-like morphologies. Furthermore, the domination of disc-like galaxy morphology in LBGs at $z \sim 1$ is in agreement with the result of Burgarella et al. (2006) for LBGs at a similar redshift range to ours: they found that 75 per cent of LBGs are compatible with such morphology. However, our result contrasts with that of Basu-Zych et al. (2011), who found that most LBGs appear to have irregular morphologies and only a few have disc-like morphologies. This difference is probably due again (see Section 5) to the inclusion in their sample of galaxies at redshifts higher than ours.

In order to obtain the physical sizes of our *GALEX*-selected LBGs we use the previous 8 arcsec × 8 arcsec *I*-band ACS cutouts and carry out fits to their radial light curves with GALFIT (Peng et al. 2010). In this step, we consider Sérsic profiles (Sersic 1968), which can be described as

$$\Sigma(r) = \Sigma_\mathrm{e} \exp\left[-\kappa\left(\left(\frac{r}{R_\mathrm{eff}}\right)^{1/n} - 1\right)\right], \quad (3)$$

where Σ_e is the pixel surface brightness at the effective radius R_eff and n is the concentration parameter or Sérsic index. The effective radius is the radius that encloses half the light of the galaxy. To

[2] http://irsa.ipac.caltech.edu/data/COSMOS/index_cutouts.html

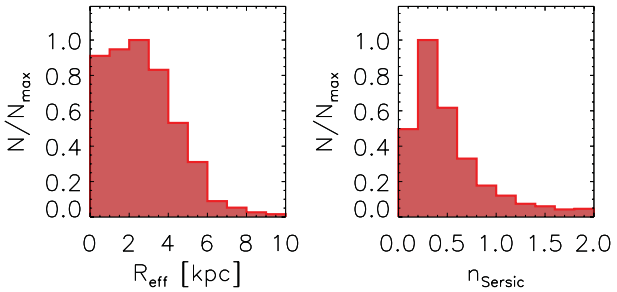

Figure 15. Distribution of the effective radii (left) and the Sérsic indices (right) for our *GALEX*-selected LBGs with available ACS images. Histograms have been normalized to their maxima in order to clarify the representations.

make this definition true, the dependent variable κ is coupled to n (Peng et al. 2010). For each input galaxy, GALFIT provides its effective radius (in pixels) and the Sérsic index, along with their uncertainties. In order to convert the effective radius in pixels into the physical size in kiloparsecs we employ the ACS pixel scale and the assumed cosmology for calculating the arcsec/pixel at the redshift of each galaxy. Fig. 15 shows the distribution of the effective radius and the Sérsic index for our *GALEX*-selected LBGs. The median effective radius for our LBGs is 2.48 kpc. The values of the Sérsic indices for LBGs are compatible with most of them being disc-like galaxies. This is in agreement with the results of the visual morphological analysis.

Shown in Fig. 16 are the relations between the physical sizes of our *GALEX*-selected LBGs and their dust-corrected total SFR and stellar mass. It can be seen that there is a trend between the physical size and both SFR and stellar mass: larger galaxies tend to form stars faster, and to have higher stellar masses. The correlation between the total SFR and the effective radius exists whatever the dust attenuation method employed. The size–stellar mass relation has also been reported to occur in LBGs at a similar and higher redshift ranges. Mosleh et al. (2012) found that the stellar mass–size relation for LBGs persists up to $z \sim 5$.

7 COLOUR–MAGNITUDE DIAGRAM

An important tool with which to analyse the properties of our *GALEX*-selected LBGs is their location in a colour–magnitude diagram (CMD). Traditionally, this kind of diagram has been used to separate local galaxies between non-SF galaxies earlier than the Sa morphological type and SF galaxies later than Sb in morphological type. In a colour space, the former tend to populate a red sequence and the latter are located in the so-called blue cloud (Strateva et al. 2001; Hogg et al. 2002). This behaviour translates into a bimodal distribution of the colour of galaxies, which allows one both to study the nature of different samples of galaxies by looking at their position in the colour space and to look for galaxies with different SF natures, by imposing conditions on their location in such a diagram. Furthermore, this bimodality in the local Universe has been proved to apply at higher redshifts, at least up to $z \sim 1.6$ (Blanton et al. 2003; Bell et al. 2004; Weiner et al. 2005; Cirasuolo et al. 2007; Franzetti et al. 2007; Williams et al. 2009; Taylor et al. 2009; Nicol et al. 2011). Following this idea, we plot in Fig. 17 the location of our *GALEX*-selected LBGs in a CMD associated with the magnitudes in the u and r broad-band filters of the SDSS survey. The apparent u and r and absolute r magnitudes are obtained by convolving the best-fitting template of each galaxy with the transmission of the u and r SDSS filters shifted in wavelength according to the redshift of each source. Along with those points we also represent a sample of SDSS local galaxies taken from the DR7 (Abazajian et al. 2009) and a sample of $z_{\rm phot}$-selected galaxies at $z \sim 1$ taken from the ALHAMBRA survey. The sample of local galaxies

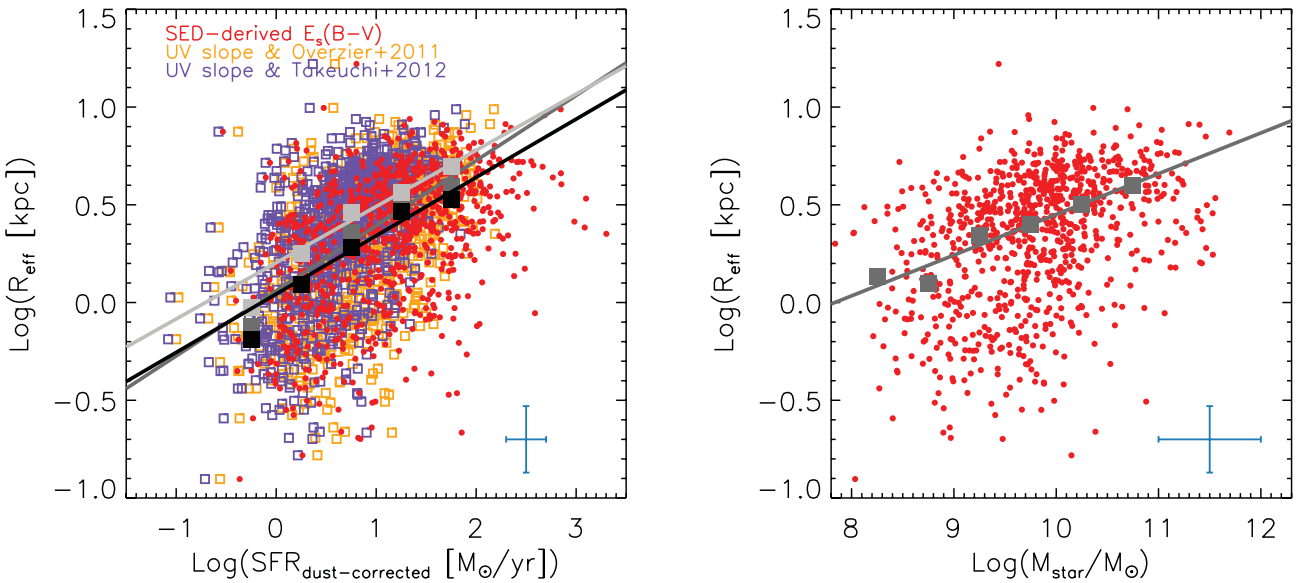

Figure 16. Left: Effective radius against the dust-corrected total SFR for our *GALEX*-selected LBGs at $z \sim 1$ with available ACS images. As indicated in the legend, we include points associated with the total SFR obtained with the SED-derived dust attenuation (red symbols) and with the UV continuum slope and the application of the Overzier et al. (2011) (orange symbols) and Takeuchi et al. (2012) (purple symbols) laws. Black, dark grey, and light grey squares represent the median values of the dust-corrected total SFR obtained with the SED-derived dust attenuation, the Overzier et al. (2011), and the Takeuchi et al. (2012) laws, respectively, for each considered bin of effective radius. Right: Effective radius against the SED-derived stellar mass for our *GALEX*-selected LBGs at $z \sim 1$ (red dots) with available ACS images. Grey squares represent the median values of the SED-derived stellar mass for each considered bin of effective radius. The grey straight line represents a linear fit to the grey squares. In both plots, the blue error bars represent the typical uncertainty in the determinations of the SED-derived dust-corrected total SFR and stellar mass (see Section 5.1) and effective radius.

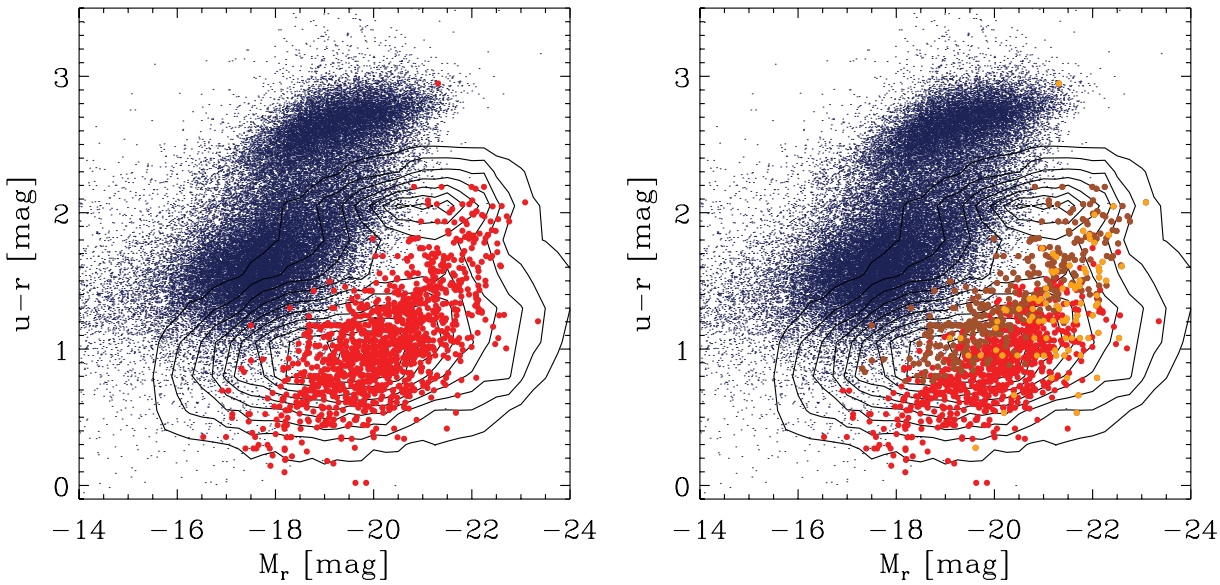

Figure 17. Left: Locus of our *GALEX*-selected LBGs (red dots) in a colour–magnitude diagram (CMD). For comparison, we represent with blue dots the locations in such a diagram of a sample of local galaxies selected from the SDSS survey. Furthermore, we represent with black contours the typical CMD for galaxies at $z \sim 1$ obtained from a general population of galaxies at that redshift taken from the ALHAMBRA survey. These contours show the location of the blue cloud, green valley, and red sequence at that redshift and clarify the discussions given in the text. Right: As for the left panel, but segregating old-LBGs (brown) and dusty-LBGs (orange). Old-LBGs are those LBGs older than 1200 Myr, while dusty-LBGs are those LBGs whose dust attenuation is higher than $E_s(B-V) = 0.4$.

comprises all the galaxies in the SDSS whose spectroscopic redshifts are below 0.035. In this case, the magnitudes plotted are those that we extract from the photometric catalogues of the SDSS survey. At such low redshifts there is no need for *K*-correction. In order to build the sample of galaxies at $z \sim 1$ we select all the galaxies in the ALHAMBRA survey (in all the already observed fields) whose photometric redshifts are around that value and whose observed *Ks*-band magnitudes are brighter than 22 mag, similar to the limits employed in Williams et al. (2009) and Taylor et al. (2009). By using the optical and NIR photometry of the ALHAMBRA survey we fit their SEDs with BC03 templates and obtain their $u - r$ colours and absolute *r*-band magnitudes in the same way as for LBGs. It can be seen in the left panel of Fig. 17 that the bimodality that is seen in the local Universe is also clearly present at $z \sim 1$. This result also indicates the power of the ALHAMBRA survey in characterizing the CMD of galaxies at different redshifts.

The majority of our *GALEX*-selected LBGs are located in the blue cloud of galaxies at their redshift, indicating that these kinds of galaxies are blue and active SF galaxies, as expected from their selection criteria in the UV. A minority of LBGs are shifted towards the red sequence or are located between the blue cloud and the red sequence, the so-called green valley. This position does not necessarily indicate that these galaxies are non-SF. Actually, it can be the case that these galaxies have redder optical colours either because of a significant amount of dust that is attenuating their bluest emitted light, and/or because there is an important contribution of old stellar populations in their SEDs, being more evolved systems. To clarify this issue we show in the right panel of Fig. 17 the position of our *GALEX*-selected LBGs in the CMD as a function of SED-derived dust attenuation and age. We arbitrarily consider two subclasses within the LBGs: those with age $\gtrsim$1200 Myr (old-LBGs) and those with age $\lesssim$1200 Myr and $E_s(B-V) \gtrsim 0.4$ (dusty-LBGs). It can be clearly seen from Fig. 17 that those LBGs that are located over the green valley or near the red sequence are old-LBGs and dusty-LBGs, whereas those LBGs whose ages are younger than 1200 Myr and have low/intermediate [$E_s(B-V) < 0.4$] dust attenuation are located over the blue cloud.

8 COMPARISON WITH HIGH-REDSHIFT LBGS

In this section we analyse the differences/similarities between LBGs at $z \sim 1$ and $z \sim 3$ in order to study whether the Lyman break selection criterion selects different kinds of galaxies at different redshifts. As noted in Section 4.2, high-redshift LBGs tend to be intrinsically brighter than those studied in this work as a consequence of the use of magnitude-limited observations. If we want to compare galaxies that are selected at different redshifts with a similar selection criterion we must limit the rest-frame UV luminosities of the samples to the same range. We use the rest-frame UV luminosities, as LBGs at any redshift are selected in the rest-frame UV. This sample was defined in Section 4.2 as UV-bright LBGs and it comprises 65 galaxies. According to their SEDs, UV-bright LBGs are less dusty, have a higher SFR, are more massive, and have a bluer UV continuum slope than the whole population of LBGs at $z \sim 1$. However, there is no significant difference in their ages, which are mostly below 500 Myr for both populations.

Fig. 18 shows the distributions of the SED-derived age, dust attenuation, and stellar mass for our UV-bright LBGs (orange histograms) and for a sample of LBGs at $z \sim 3$ studied in Papovich, Dickinson & Ferguson (2001) (green histograms). UV-bright LBGs at $z \sim 1$ have ages distributed mainly between 1 and 400 Myr with a median value of 171 Myr, whereas LBGs at $z \sim 3$ are younger galaxies with a median age of 36 Myr. The difference in the median values is of the same order as the uncertainties of the SED-derived age at $z \sim 1$. However, as can be seen in the histogram shown in Fig. 18, at $z \sim 1$ there is a presence of older stellar populations (with ages mainly between 150 and 400 Myr) than at $z \sim 3$. A Kolmogorov–Smirnov test applied to both histograms gives a very low probability that they represent similar distributions. This could indicate that the galaxies selected with the Lyman break criterion at

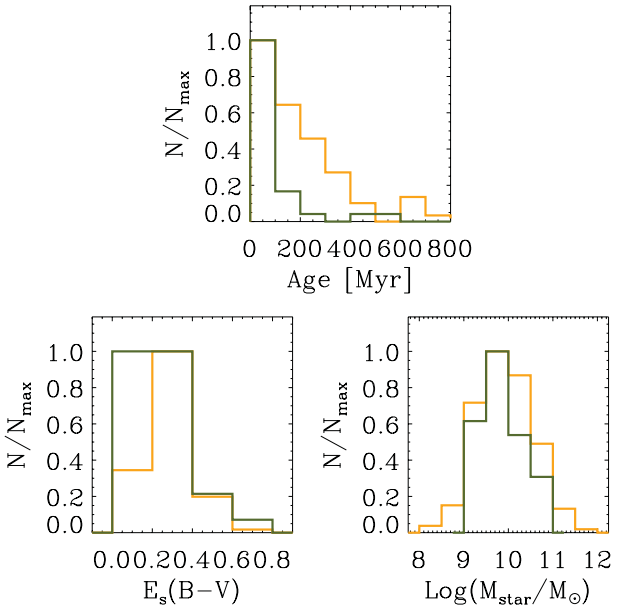

Figure 18. Distribution of the SED-derived age, dust attenuation, and stellar mass for our UV-bright LBGs (orange histograms) and high-redshift LBGs (green histograms) taken from Papovich et al. (2001). Histograms have been normalized to their maxima in order to clarify the representations.

$z \sim 1$ are at a later evolutionary stage than those at $z \sim 3$. It should be noted that, as pointed out in many previous works and in Section 5, the uncertainties of the SED-derived stellar age are usually high and, furthermore, the age evolution found can be the consequence of diverse factors: (i) using different SFHs in the analysis of the SED of the galaxies; (ii) employing photometric information with different wavelength coverages; (iii) the degeneracy between dust attenuation, metallicity, and age, etc. Therefore, the previous evidence of an evolution of the age of LBGs with redshift is not conclusive and should be confirmed in further studies with a more detailed study of the rest-frame UV-to-NIR SED of these galaxies.

The dust attenuation distribution of LBGs at $z \sim 1$ seems to contain lower values than the distribution at high redshift, although both have median values of $E_s(B-V) = 0.25$. The typical uncertainty of the SED-derived dust attenuation in our work is $\Delta E_s(B-V) = 0.1$ (see Section 5). This value along with the similar median values of the distributions at $z \sim 1$ and $z \sim 3$ prevent us from constraining any evolution of the median values of dust attenuation of LBGs with redshift. This can be an effect of the procedure employed. An SED-fitting technique is not precise enough to constrain an evolution of dust attenuation with redshift, and other techniques should be employed. The direct measurement of dust emission of LBGs in the FIR could give clues for addressing this issue.

Regarding stellar masses, it can be seen that the distributions at $z \sim 1$ and $z \sim 3$ span a similar range. The median values of the stellar mass of our UV-bright LBGs and LBGs at $z \sim 3$ are $\log(M_*/\mathrm{M}_\odot) = 10.0$ and $\log(M_*/\mathrm{M}_\odot) = 9.7$, respectively. This difference is similar to the typical uncertainties of the stellar mass determinations performed in this work, and therefore we cannot constrain any evolution in the stellar mass of LBGs with redshift either. The median value of the stellar mass found in the present work is between those reported in Magdis et al. (2010) for IRAC-8μm detected LBGs and IRAC-8 μm faint LBGs at $z \sim 3$, namely $\langle \log M_*/\mathrm{M}_\odot \rangle = 11$ and $\langle \log M_*/\mathrm{M}_\odot \rangle = 9$, respectively.

Regarding the UV continuum slope, UV-bright LBGs have a median value of $\beta = -1.44$. This value is larger (redder) than those reported at higher redshifts (Lehnert & Bremer 2003; Bouwens et al. 2006; Hathi et al. 2008; Bouwens et al. 2009; Wilkins et al. 2011; Bouwens et al. 2011; Castellano et al. 2012), indicating that LBGs at lower redshifts tend to be redder in the UV continuum than those at higher redshifts. The UV continuum slope is not a parameter associated directly with the BC03 templates, but it is obtained once the best-fitting BC03 template for each galaxy is known. Consequently, this parameter is more insensitive to the various SFHs adopted for building the BC03 template, and therefore is a good and accurate indicator of the evolution of LBGs with redshift.

Mosleh et al. (2011) studied the redshift evolution of the physical sizes of samples of LBGs and other UV/submm-selected galaxies at different redshifts and found that their size increases with decreasing redshift. Mosleh et al. (2012) studied the redshift evolution of LBGs from $z \sim 1$ up to $z \sim 7$ and found that the median size of LBGs at a given stellar mass increases towards lower redshifts. The median size of our sample of UV-bright LBGs is 2.92 kpc. Mosleh et al. (2012) studied the redshift evolution of LBGs considering galaxies in two bins of stellar mass: $8.6 < \log(M_*/\mathrm{M}_\odot) < 9.5$ and $9.5 < \log(M_*/\mathrm{M}_\odot) < 10.4$. As indicated above, the median value of the stellar mass of our UV-bright LBGs is $\log(M_*/\mathrm{M}_\odot) = 10.0$. The median value of the size of UV-bright LBGs is slightly lower than those presented in Mosleh et al. (2012) and Mosleh et al. (2011) for the corresponding stellar mass range. This small difference is probably because, although these authors also work with *GALEX*-selected LBGs, they consider galaxies located within $0.6 < z < 1.4$, whereas we limit the redshift of our sample to $z > 0.8$. The inclusion of galaxies at lower redshifts might increase the median value of the size, explaining the difference found between the two works.

It is important to remark again that there is a fundamental difference in the selection criteria for LBGs at different redshifts. Given that the combination of *GALEX* and ALHAMBRA (including IRAC for a subsample) provides very accurate photometric redshifts for our galaxies, we do not need any extra condition to rule out interlopers. However, this is not the case at high redshifts. At $z \gtrsim 2$, the photometric redshifts of the sources are not accurate enough to ensure a proper cleaning of the sample from interlopers. As a consequence, additional criteria should be applied. These extra criteria usually involve limits in the observed optical colours of the samples. For example, as discussed in Madau et al. (1996) for their sample of F300W dropouts, the application of extra criteria rules out interlopers that are in another redshift range, but they also missed galaxies at the proper redshift at the same time. The missing galaxies tend to be redder than those included in the final sample, either because they are older or because they are attenuated by dust. Therefore, it is clear that the additional criteria employed at high redshift discard of certain kinds of subclasses of galaxies at each redshift. In contrast, in our work, as in Burgarella et al. (2006, 2007), we do not apply any extra observed optical colour criteria and therefore we include in the sample all kinds of galaxies that have a break between the FUV and NUV filters, regardless of their age, dust attenuation or optical colour.

All previous results seem to indicate that LBGs at $z \sim 1$ tend to be older, to be bluer in their UV continuum, and to have larger sizes than those at higher redshifts. Therefore, SED fitting and morphological studies indicate that LBGs at lower redshifts are at a later evolutionary stage than those at higher redshifts. It should be noted that these differences between LBGs at different redshifts were found by comparing the results obtained in this work with those from previous studies performed by other authors. Therefore, this comparison might suffer from uncertainties arising from the

different methods employed in each work or from slightly different selection criteria, for example the use of BC03 templates associated with different SFHs or different photometric coverage of the SEDs of galaxies at different redshifts. Thus, in order to properly characterize the evolution of LBGs with redshift a more precise work should be undertaken in which the photometric SEDs of the galaxies are sampled over the same rest-frame wavelength range, and the selection criteria and the procedures employed for the analysis of the physical properties of the galaxies are as similar as possible.

9 CONCLUSIONS

In this work we have analysed the physical properties derived from the SED-fitting of a sample of 1225 *GALEX*-selected LBGs at $0.8 \lesssim z \lesssim 1.2$ by using a combination of UV and optical/NIR data coming from *GALEX* observations and the ALHAMBRA survey, respectively. ALHAMBRA uses a set of 20 medium-band (width $\sim$300 Å) optical and the three classical NIR *JHKs* filters to cover the observed optical SED of galaxies in an unprecedented way. This provides a good sampling of both the UV continuum slope and the Balmer break, increasing significantly the accuracy of the results of the SED-fitting technique. We defined LBGs as those galaxies that have a difference of colour greater than 1.5 mag between the FUV and NUV filters of the *GALEX* satellite. Our main conclusions are as follows.

(i) According to the SED-fitting with BC03 templates built assuming a constant SFR, Salpeter IMF, and metallicity $Z = 0.2\,Z_{\odot}$, *GALEX*-selected LBGs at $z \sim 1$ are young galaxies with ages mostly younger than 300 Myr, with a median dust attenuation of $E_s(B-V)$ of 0.20, and a median UV continuum slope of -1.53. As a consequence of the selection criteria used they are UV-bright objects with UV-uncorrected SFRs of about $2.0\,M_{\odot}\,yr^{-1}$. When dust-correcting their rest-frame UV luminosity, their total SFR turns out to have a median value of $46.4\,M_{\odot}\,yr^{-1}$. Combining the total SFRs and ages, we find that *GALEX*-selected LBGs have a median stellar mass of $\log(M_*/M_{\odot}) = 9.74$. Only 2 per cent of the galaxies selected with the Lyman break selection criterion have an AGN, according to their X-ray emission.

(ii) LBGs with higher stellar masses have higher total SFRs and lower values of the specific SFR. The anticorrelation between the specific SFR and stellar mass supports the downsizing scenario, whereby more massive galaxies formed their stars earlier and faster than galaxies with a lower stellar mass.

(iii) Morphologically, LBGs at $z \sim 1$ are mostly disc-like galaxies (about 69 per cent), while those remaining are interacting, compact or irregular systems in much lower percentages. This is confirmed by their Sérsic indices, which are typically below 0.5. The median effective radius for our *GALEX*-selected LBGs at $z \sim 1$ is 2.48 kpc. Larger galaxies tend to have higher total SFRs and stellar masses.

(iv) In a CMD, most *GALEX*-selected LBGs are located over the blue cloud at their redshift, which indicates that they are active SF galaxies. Some LBGs are located over the green valley or near the red sequence. They turn out to be the dustiest and/or oldest galaxies in the samples, signs that they are more evolved systems.

(v) Comparing with their high-redshift analogues, we find that the galaxies selected through the Lyman break criterion at $z \sim 1$ seem to be at a later evolutionary stage than those at high redshifts. However, the uncertainties in the SED-derived age are typically significant, and consequently the age evolution should be confirmed with a more detailed study of the rest-frame UV-to-NIR SEDs of LBGs at different redshifts. We do not find any significant difference in the distributions of stellar mass or dust attenuation for LBGs at high and intermediate redshifts. LBGs at lower redshifts are larger, have a greater contribution of older stellar population to their SEDs, and are redder in their UV continuum than their high-redshift analogues.

ACKNOWLEDGEMENTS

The authors would like to thank the referee for the careful reading of the manuscript and for valuable feedback that has improved the presentation of our results. I. Oteo would also like to thank Professor Tsutomu T. Takeuchi for kindly providing useful comments. This research has been supported by the Spanish Ministerio de Econom'a y Competitividad (MINECO) under grant AYA2011-29517-C03-01. Some/all of the data presented in this paper were obtained from the Multimission Archive at the Space Telescope Science Institute (MAST). STScI is operated by the Association of Universities for Research in Astronomy, Inc., under NASA contract NAS5-26555. Support for MAST for non-*HST* data is provided by the NASA Office of Space Science via grant NNX09AF08G and by other grants and contracts. This work is based on observations made with the European Southern Observatory telescopes obtained from the ESO/ST-ECF Science Archive Facility and from zCOSMOS observations carried out using the Very Large Telescope at the ESO Paranal Observatory under Programme ID: LP175.A-0839.

Funding for the SDSS and SDSS-II was provided by the Alfred P. Sloan Foundation, the Participating Institutions, the National Science Foundation, the US Department of Energy, the National Aeronautics and Space Administration, the Japanese Monbukagakusho, the Max Planck Society, and the Higher Education Funding Council for England. The SDSS web site is http://www.sdss.org/.

The SDSS is managed by the Astrophysical Research Consortium for the Participating Institutions. The Participating Institutions are the American Museum of Natural History, the Astrophysical Institute Potsdam, the University of Basel, the University of Cambridge, the Case Western Reserve University, the University of Chicago, Drexel University, Fermilab, the Institute for Advanced Study, the Japan Participation Group, Johns Hopkins University, the Joint Institute for Nuclear Astrophysics, the Kavli Institute for Particle Astrophysics and Cosmology, the Korean Scientist Group, the Chinese Academy of Sciences (LAMOST), Los Alamos National Laboratory, the Max-Planck-Institute for Astronomy (MPIA), the Max-Planck-Institute for Astrophysics (MPA), New Mexico State University, Ohio State University, the University of Pittsburgh, the University of Portsmouth, Princeton University, the United States Naval Observatory, and the University of Washington. Financial support from the Spanish grant AYA2010-15169 and from the Junta de Andalucia through TIC-114 and the Excellence Project P08-TIC-03531 is acknowledged.

REFERENCES

Abazajian K. N. et al., 2009, ApJS, 182, 543
Adelberger K. L., Steidel C. C., Shapley A. E., Hunt M. P., Erb D. K., Reddy N. A., Pettini M., 2004, ApJ, 607, 226
Aparicio Villegas T. et al., 2010, AJ, 139, 1242
Barger A. J., Cowie L. L., Wang W.-H., 2008, ApJ, 689, 687
de Barros S., Schaerer D., Stark D. P., 2012, preprint (arXiv:1207.3663)
Basu-Zych A. R., Hornschemeier A. E., Hoversten E. A., Lehmer B., Gronwall C., 2011, ApJ, 739, 98
Bell E. F. et al., 2004, ApJ, 608, 752
Benítez N. et al., 2009, ApJ, 692, L5
Blanton M. R. et al., 2003, ApJ, 594, 186

Bongiovanni A. et al., 2010, A&A, 519, L4
Bouwens R. J., Illingworth G. D., Blakeslee J. P., Franx M., 2006, ApJ, 653, 53
Bouwens R. J. et al., 2009, ApJ, 705, 936
Bouwens R. J. et al., 2010a, ApJ, 708, L69
Bouwens R. J. et al., 2010b, ApJ, 708, L69
Bouwens R. J. et al., 2011, ApJ, 737, 90B
Bouwens R. J. et al., 2012, ApJ, 754, 83B
Bruzual G., Charlot S., 2003, MNRAS, 344, 1000 (BC03)
Bunker A. J., Stanway E. R., Ellis R. S., McMahon R. G., 2004, MNRAS, 355, 374
Burgarella D. et al., 2006, A&A, 450, 69
Burgarella D., Le Floc'h E., Takeuchi T. T., Huang J. S., Buat V., Rieke G. H., Tyler K. D., 2007, MNRAS, 380, 986
Burgarella D. et al., 2011, ApJ, 734, L12
Calzetti D., Kinney A. L., Storchi-Bergmann T., 1994, ApJ, 429, 582
Calzetti D., Armus L., Bohlin R. C., Kinney A. L., Koornneef J., Storchi-Bergmann T., 2000, ApJ, 533, 682
Capak P. et al., 2007, ApJS, 172, 99
Castellano M. et al., 2012, A&A, 540, A39
Chen Z., Shu C. G., Burgarella D., Buat V., Huang J.-S., Luo Z. J., 2013, MNRAS, 431, 2080
Cirasuolo M. et al., 2007, MNRAS, 380, 585
Cowie L. L., Hu E. M., 1998, AJ, 115, 1319
Cowie L. L., Barger A. J., Hu E. M., 2010, ApJ, 711, 928
Cristóbal-Hornillos D. et al., 2009, ApJ, 696, 1554
Daddi E., Cimatti A., Renzini A., Fontana A., Mignoli M., Pozzetti L., Tozzi P., Zamorani G., 2004, ApJ, 617, 746
Daddi E. et al., 2007, ApJ, 670, 156
Damen M., Förster Schreiber N. M., Franx M., Labbé I., Toft S., van Dokkum P. G., Wuyts S., 2009, ApJ, 705, 617
Dunlop J. S., McLure R. J., Robertson B. E., Ellis R. S., Stark D. P., Cirasuolo M., de Ravel L., 2012, MNRAS, 420, 901
Dunne L. et al., 2009, MNRAS, 394, 3
Elbaz D. et al., 2007, A&A, 468, 33
Elbaz D. et al., 2011, A&A, 533, A119
Elmegreen B. G., Elmegreen D. M., Fernandez M. X., Lemonias J. J., 2009, ApJ, 692, 12
Elvis M. et al., 2009, ApJS, 184, 158
Erb D. K., Steidel C. C., Shapley A. E., Pettini M., Reddy N. A., Adelberger K. L., 2006, ApJ, 647, 128
Feldmann R. et al., 2006, MNRAS, 372, 565
Feulner G., Goranova Y., Drory N., Hopp U., Bender R., 2005, MNRAS, 358, L1
Finkelstein S. L., Rhoads J. E., Malhotra S., Grogin N., Wang J., 2008, ApJ, 678, 655
Finkelstein S. L., Cohen S. H., Malhotra S., Rhoads J. E., 2009a, ApJ, 700, 276
Finkelstein S. L., Rhoads J. E., Malhotra S., Grogin N., 2009b, ApJ, 691, 465
Finkelstein S. L., Rhoads J. E., Malhotra S., Grogin N., 2009c, ApJ, 691, 465
Finkelstein S. L., Papovich C., Giavalisco M., Reddy N. A., Ferguson H. C., Koekemoer A. M., Dickinson M., 2010a, ApJ, 719, 1250
Finkelstein S. L., Papovich C., Giavalisco M., Reddy N. A., Ferguson H. C., Koekemoer A. M., Dickinson M., 2010b, ApJ, 719, 1250
Finkelstein S. L. et al., 2012, ApJ, 756, 164
Franzetti P. et al., 2007, A&A, 465, 711
Gawiser E. et al., 2006, ApJ, 642, L13
Gawiser E. et al., 2007, ApJ, 671, 278
Giavalisco M. et al., 2004, ApJ, 600, L103
González V., Labbé I., Bouwens R. J., Illingworth G., Franx M., Kriek M., Brammer G. B., 2010, ApJ, 713, 115
Gronwall C. et al., 2007, ApJ, 667, 79
Guaita L. et al., 2011, ApJ, 733, 114
Guillaume M., Llebaria A., Aymeric D., Arnouts S., Milliard B., 2006, in Dougherty E. R., Astola J. T., Egiazarian K. O., Nasrabadi N. M., Rizvi S. A., eds, Society of Photo-Optical Instrumentation Engineers (SPIE) Conf. Ser. Vol. 6064, Image Processing: Algorithms and Systems, Neural Networks, and Machine Learning. SPIE, p. 332
Haberzettl L., Williger G., Lehnert M. D., Nesvadba N., Davies L., 2012, ApJ, 745, 96
Hathi N. P., Malhotra S., Rhoads J. E., 2008, ApJ, 673, 686
Hathi N. P. et al., 2010, ApJ, 720, 1708
Hathi N. P. et al., 2013, ApJ, 765, 88
Hibon P., Malhotra S., Rhoads J., Willott C., 2011, ApJ, 741, 101
Hibon P., Kashikawa N., Willott C., Iye M., Shibuya T., 2012, ApJ, 744, 89
Hogg D. W. et al., 2002, AJ, 124, 646
Iwata I., Ohta K., Tamura N., Akiyama M., Aoki K., Ando M., Kiuchi G., Sawicki M., 2007, MNRAS, 376, 1557
Karim A. et al., 2011, ApJ, 730, 61
Kennicutt R. C., Jr, 1998, ARA&A, 36, 189
Kong X., Charlot S., Brinchmann J., Fall S. M., 2004, MNRAS, 349, 769
Lai K. et al., 2008, ApJ, 674, 70
Lehmer B. D. et al., 2005, AJ, 129, 1
Lehnert M. D., Bremer M., 2003, ApJ, 593, 630
Lilly S. J. et al., 2007, ApJS, 172, 70
Ly C. et al., 2009, ApJ, 697, 1410
Ly C., Malkan M. A., Hayashi M., Motohara K., Kashikawa N., Shimasaku K., Nagao T., Grady C., 2011, ApJ, 735, 91
Madau P., 1995, ApJ, 441, 18
Madau P., Ferguson H. C., Dickinson M. E., Giavalisco M., Steidel C. C., Fruchter A., 1996, MNRAS, 283, 1388
Magdis G. E., Rigopoulou D., Huang J.-S., Fazio G. G., 2010, MNRAS, 401, 1521
Martin D. C. et al., 2005, ApJ, 619, L1
Matute I. et al., 2012, A&A, 542A, 20M
Meurer G. R., Heckman T. M., Lehnert M. D., Leitherer C., Lowenthal J., 1997, AJ, 114, 54
Meurer G. R., Heckman T. M., Calzetti D., 1999, ApJ, 521, 64
Moles M. et al., 2005, preprint (astro-ph/0504545)
Moles M. et al., 2008, AJ, 136, 1325
Mosleh M., Williams R. J., Franx M., Kriek M., 2011, ApJ, 727, 5
Mosleh M. et al., 2012, ApJ, 756, L12
Murayama T. et al., 2007, ApJS, 172, 523
Nandra K., Mushotzky R. F., Arnaud K., Steidel C. C., Adelberger K. L., Gardner J. P., Teplitz H. I., Windhorst R. A., 2002, ApJ, 576, 625
Nicol M.-H., Meisenheimer K., Wolf C., Tapken C., 2011, ApJ, 727, 51
Nilsson K. K. et al., 2007, A&A, 471, 71
Nilsson K. K., Tapken C., Møller P., Freudling W., Fynbo J. P. U., Meisenheimer K., Laursen P., Östlin G., 2009, A&A, 498, 13
Nilsson K. K., Möller-Nilsson O., Rosati P., Lombardi M., Kümmel M., Kuntschner H., Walsh J. R., Fosbury R. A. E., 2011, A&A, 526, A10
Noeske K. G. et al., 2007, ApJ, 660, L43
Oke J. B., Gunn J. E., 1983, ApJ, 266, 713
Oteo I. et al., 2011, ApJ, 735, L15
Oteo I. et al., 2012a, A&A, 541, A65
Oteo I. et al., 2012b, ApJ, 751, 1390
Oteo I. et al., 2013a, A&A, 554L, 3O
Oteo I. et al., 2013b, MNRAS, preprint (arXiv:1306.1121)
Ouchi M. et al., 2008, ApJS, 176, 301
Ouchi M. et al., 2010, ApJ, 723, 869
Overzier R. A. et al., 2008, ApJ, 673, 143
Overzier R. A. et al., 2011, ApJ, 726, L7
Pannella M. et al., 2009, ApJ, 698, L116
Papovich C., Dickinson M., Ferguson H. C., 2001, ApJ, 559, 620
Peng C. Y., Ho L. C., Impey C. D., Rix H., 2010, AJ, 139, 2097
Pirzkal N., Malhotra S., Rhoads J. E., Xu C., 2007, ApJ, 667, 49
Pović M. et al., 2009, ApJ, 706, 810
Pović M. et al., 2012, A&A, 541A, 118P
Rix H.-W. et al., 2004, ApJS, 152, 163
Rodighiero G. et al., 2010, A&A, 518, L25
Salim S. et al., 2007, ApJS, 173, 267
Salpeter E. E., 1955, ApJ, 121, 161

Salvato M. et al., 2011, ApJ, 742, 61
Sersic J. L., 1968, in Sersic J. L., ed., Atlas de Galaxias Australes. Observatorio Astronomico, Cordoba, Argentina
Shioya Y. et al., 2009, ApJ, 696, 546
Stanway E. R., Bunker A. J., McMahon R. G., 2003, MNRAS, 342, 439
Steidel C. C., Giavalisco M., Dickinson M., Adelberger K. L., 1996, AJ, 112, 352
Steidel C. C., Adelberger K. L., Giavalisco M., Dickinson M., Pettini M., 1999, ApJ, 519, 1
Steidel C. C., Adelberger K. L., Shapley A. E., Pettini M., Dickinson M., Giavalisco M., 2003, ApJ, 592, 728
Strateva I. et al., 2001, AJ, 122, 1861
Takeuchi T. T., Yuan F.-T., Ikeyama A., Murata K. L., Inoue A. K., 2012, ApJ, 755, 144
Taylor E. N. et al., 2009, ApJ, 694, 1171
Verma A., Lehnert M. D., Förster Schreiber N. M., Bremer M. N., Douglas L., 2007, MNRAS, 377, 1024
Weiner B. J. et al., 2005, ApJ, 620, 595
Wilkins S. M., Bunker A. J., Stanway E., Lorenzoni S., Caruana J., 2011, MNRAS, 417, 717
Williams R. J., Quadri R. F., Franx M., van Dokkum P., Labbé I., 2009, ApJ, 691, 1879
Wolf C., Meisenheimer K., Röser H.-J., 2001, A&A, 365, 660
Wolf C. et al., 2004, A&A, 421, 913
Wolf C. et al., 2005, ApJ, 630, 771
Yabe K., Ohta K., Iwata I., Sawicki M., Tamura N., Akiyama M., Aoki K., 2009, ApJ, 693, 507

This paper has been typeset from a TEX/LATEX file prepared by the author.